Oxygen isotope study of the Asuka-881020 CH chondrite I: Non-porphyritic chondrules

Daisuke Nakashima[1,2,*], Makoto Kimura[3,4], Kouichi Yamada[4], Takaaki Noguchi[5], Takayuki Ushikubo[2,6], and Noriko Kita[2]

[1]Department of Earth and Planetary Material Sciences, Faculty of Science, Tohoku University, Aoba, Sendai, Miyagi 980-8578, Japan.
[2]Department of Geoscience, University of Wisconsin-Madison, Madison, WI 53706, USA
[3]National Institute of Polar Research, Tokyo 190-8518, Japan
[4]Faculty of Science, Ibaraki University, Mito, Ibaraki, 310-8512, Japan
[5]Faculty of Arts and Science, Kyushu University, 744 Motooka, Nishi-ku, Fukuoka 819-0395, Japan
[6]Kochi Institute for Core Sample Research, JAMSTEC, Monobe-otsu 200, Nankoku, Kochi 783-8502, Japan

*Corresponding author, Tel/Fax: +81-22-795-5903, Email: dnaka@tohoku.ac.jp

Submitted to Geochimica Cosmochimica et Acta
Abstract: 413 words
Main text: ~ 9000 words

Abstract

We measured oxygen isotope ratios and major elemental compositions of non-porphyritic chondrules and lithic fragments with various textures and chemical compositions in the Asuka-881020 CH chondrite. The oxygen isotope ratios plot along the primitive chondrule mineral line with $\Delta^{17}O$ (= $\delta^{17}O - 0.52 \times \delta^{18}O$) values from ~ –21‰ to +5‰. The $\Delta^{17}O$ values increase with decreasing Mg# (= molar [MgO]/[MgO+FeO]%) from 99.6 to 58.5, similarly to the $\Delta^{17}O$-Mg# trends for the chondrules in other carbonaceous chondrites.

Most of the measured objects (non-porphyritic chondrules and lithic fragments) including chondrules analyzed in the previous studies are classified into three groups based on the $\Delta^{17}O$ values and chemistry; the –2.3‰ group with FeO-poor compositions (the most abundant group), the +1.4‰ group with FeO-rich compositions, and the –6.3‰ group with FeO-poor compositions. Skeletal olivine and magnesian cryptocrystalline (MgCC) chondrules and MgCC chondrule fragments, which are the –2.3‰ group objects, may have formed via fractional condensation in the isotopically uniform gaseous environment with $\Delta^{17}O$ of –2.3‰. When silica-normative materials condensed from gas at ~ 1200 K, ^{16}O-rich refractory solids, similar to Ca-Al-rich inclusions, were incorporated into the environment. The silica-normative materials that condensed onto the ^{16}O-rich refractory solids were reheated at 1743 – 1968 K and formed cristobalite-bearing chondrules with $\Delta^{17}O$ of ~ –6‰. This scenario can explain the absence of silica-bearing chondrules in the –2.3‰ group and refractory element abundances in the cristobalite-bearing chondrules as high as those in the MgCC chondrules.

Refractory element abundances of the +1.4‰ group objects decrease from FeO-Al-rich and ferroan CC (FeCC) chondrules to FeCC chondrule fragments to FeNi metal-bearing to silica-bearing chondrules. This suggests the formation via fractional condensation in the isotopically uniform gaseous environment. The $\Delta^{17}O$ values and FeO-rich compositions of this group could be explained by an addition of ^{16}O-poor water ice as an oxidant to the relatively ^{16}O-rich solids with $\Delta^{17}O$ of –2.3‰, which may also explain existence of some MgCC chondrules and fragments with intermediate $\Delta^{17}O$ values between –2.3‰ and +1.4‰. The immiscibility textures in the silica-bearing chondrules suggest a reheating event at a temperature of > 1968 K after condensation of silica-normative materials. Thus, the non-porphyritic chondrules and fragments in CH and CB chondrites, which are classified into three distinct $\Delta^{17}O$ groups, require multiple chondrule-forming environments and heating events. Energy source for the heating events could be either impact plume and/or other dynamical processes in the protoplanetary disk, though a single heating event would not fully explain observed chemical and isotope signatures in these non-porphyritic chondrules.

1. Introduction

Among carbonaceous chondrite groups, CH and CB metal-rich carbonaceous chondrites are unique meteorite groups in terms of high abundance of FeNi metal (≥ 20 vol%), lack of fine-grained matrix, depletion in volatile lithophile elements, enrichment of refractory siderophile elements, and isotopically heavy nitrogen with a $\delta^{15}N$ variation from ~ +200‰ to +1000‰ in bulk samples (e.g., Weisberg et al., 1995, 2001; Krot et al., 2002; Scott and Krot, 2003). Metal-rich carbonaceous chondrites are divided into two groups based on the FeNi metal abundance: high-metal (CH) (~ 20 vol%) and Bencubbin-like (CB) (≥ 40 vol%). Moreover, CB chondrites are subdivided into two subgroups: CB_a (~ 40 – 60 vol% FeNi metal) and CB_b (> 70 vol% FeNi metal) (Weisberg et al., 2001; Krot et al., 2002). The CH, CB_a, and CB_b chondrites have similar bulk oxygen three-isotope ratios in $\delta^{18}O$ and $\delta^{17}O$ values (deviation of $^{18}O/^{16}O$ and $^{17}O/^{16}O$ ratios from Vienna Standard Mean Ocean Water in parts per thousands, known as VSMOW-scale; Baertschi, 1976; Clayton and Mayeda, 1999; Weisberg et al., 2001). Thus, CH and CB chondrites share multiple properties and a genetic link between the two chondrite groups has been suggested (Weisberg et al., 1995; Krot et al., 2002; Ivanova et al., 2008).

The relative abundance of chondrule textural types in CH and CB chondrites is different from those in other chondrite groups. Approximately 80% of chondrules in CH chondrites are non-porphyritic types such as cryptocrystalline (CC) and skeletal olivine (SO) and ~ 99% of chondrules in CB chondrites are CC and SO chondrules. On the other hand, more than 80% of chondrules in other chondrite groups are of porphyritic type (Scott and Krot, 2003). Most of the CC chondrules are magnesian (FeO-poor) with Mg# ≥ 90 (= molar [MgO]/[MgO+FeO]%) and are depleted in refractory and volatile elements (Scott, 1988; Krot et al., 2000, 2001a, 2010; Nakashima et al., 2011). Depletion in volatile elements including Na and K in the magnesian CC chondrules suggests that the CC chondrules were isolated from the formation location at elevated temperatures and cooled rapidly (Krot et al., 2001a; Hezel et al., 2003). Abundances of refractory elements such as Ca, Al, and Ti in the magnesian CC chondrules are also depleted to variable degree (Krot et al., 2000, 2001a), which is explained by fractional condensation, i.e., more refractory elements condense earlier in the cooling environment of solar composition and the condensates are isolated from the reactive environment (Petaev and Wood, 1998; Krot et al., 2001a; Hezel et al., 2003). The SO chondrules, which are enriched in refractory elements relative to the CC chondrules, may have formed prior to CC chondrules during fractional condensation (Krot et al., 2001a). Although some works pointed out that simple melt condensation from a gaseous plume could not explain major and trace element compositions and Mg isotope ratios of SO and CC chondrules (Gounelle et al., 2007; Fedkin et al., 2015; Oulton et al., 2016). The magnesian CC chondrules in CH and CB chondrites have nearly identical oxygen isotope ratios with $\Delta^{17}O$ (= $\delta^{17}O - 0.52 \times \delta^{18}O$) values of ~ –2.2‰ (Krot et al., 2010; Nakashima et al., 2011). It is suggested that the magnesian CC chondrules in CH and CB chondrites formed from an isotopically uniform gaseous reservoir generated by a single-stage heating event; a large-scale impact (Krot et al., 2010; Nakashima et al., 2011) or a highly energetic thermal event in a dusty region of the solar nebula (e.g., Petaev et al., 2001). Similar impact formation models are proposed for chondrules in other chondrites (e.g., Sanders and Scott, 2018). Furthermore, formation models such as heating by shock waves in a nebular setting are also proposed (e.g., Ciesla, 2005).

A subset of CC chondrules in CH chondrites contain FeNi metal with rounded-to-euhedral

texture and/or silica, which are suggested to have formed along with metal- and silica-free CC chondrules (Krot et al., 2000; Hezel et al., 2003). This hypothesis can be tested by oxygen isotope analyses of the metal- and silica-bearing CC chondrules.

Multiple in-situ analyses of chondrules in Acfer 094 (ungrouped C3.0) using secondary ion mass spectrometry (SIMS) revealed that oxygen isotope ratios of chondrules are in most cases internally homogeneous, except for relict grains that have distinct oxygen isotope ratios (Ushikubo et al., 2012). The homogeneous oxygen isotope ratios represent oxygen isotope ratios of chondrule-forming environments. Furthermore, chondrules in Acfer 094 have bimodal $\Delta^{17}O$ values of ~ −5‰ and −2‰ that negatively correlate with the Mg# values of chondrule phenocrysts, suggesting the former presence of two separate isotope reservoirs with different redox states in the disk.

Subsequent to the study of Acfer 094 chondrules, oxygen isotope systematics of chondrules in various carbonaceous chondrites were examined. The primitive carbonaceous chondrites show similar systematic trends between Mg# and $\Delta^{17}O$ values, although the detailed trends are specific to individual chondrite groups (Connolly and Huss, 2010; Rudraswami et al., 2011; Schrader et al., 2013, 2014, 2017; Tenner et al., 2013, 2015, 2017, 2018; Davidson et al., 2014; Chaumard et al., 2018; Hertwig et al., 2018, 2019a, 2019b; Yamanobe et al., 2018). One can expect that the non-porphyritic chondrules in CH and CB chondrites also show a similar $\Delta^{17}O$-Mg# trend. Krot et al. (2010) and Nakashima et al. (2011) analyzed the non-porphyritic chondrules in CH and CB chondrites for oxygen isotopes, although these works were limited to magnesian non-porphyritic chondrules. To understand oxygen isotope ratios and redox conditions of the chondrule formation environments, oxygen isotope systematics of chondrules with the full range of Mg# values, including ferroan (FeO-rich) non-porphyritic chondrules, is required.

In this study, we analyzed oxygen isotope ratios and major element compositions of magnesian and ferroan non-porphyritic chondrules and related lithic fragments in the Asuka-881020 CH chondrite (Noguchi et al., 2004; Nakamura et al., 2006) for (1) revealing a genetic link between the CC chondrules and other non-porphyritic chondrules and (2) understanding oxygen isotope reservoirs and redox conditions in the formation environments of the non-porphyritic chondrules. Lithic fragments, which are referred to as silicate fragments (Scott, 1988) and isolated particles (Grossman et al., 1988), occur around chondrules and FeNi metal, and comprise ~ 70% of CH chondrites (Scott, 1988). Lithic fragments with chemical compositions similar to those of CC chondrules were analyzed for oxygen isotopes to test the hypothesis that, in CH chondrites, lithic fragments are fragments of chondrules (Scott, 1988; Weisberg et al., 1988).

2. Analytical procedures

2.1. Electron microscopy

We used a polished thin section of the Asuka-881020 CH chondrite (51-1; National Institute of Polar Research). Chondrules and lithic fragments in the sections were examined using a scanning electron microscope (SEM; Hitachi S3400) at the University of Wisconsin-Madison and backscattering electron (BSE) images were obtained. Major elemental compositions of the chondrules and lithic fragments were measured using electron probe microanalyzers (EPMAs) at Ibaraki University (JEOL JXA-733), at National Institute of Polar Research (NIPR; JEOL JXA-8200), and at the University of Wisconsin-Madison (CAMECA SX-51) equipped with

wavelength-dispersive X-ray spectrometers (WDSs). At Ibaraki University, WDS quantitative chemical analyses of bulk chondrules were performed at 15 kV accelerating voltage and 6 nA beam current with a defocused beam of 5 - 40 μm. After correction by the Bence-Albee method, the chondrule data were recalculated by the method of Ikeda (1980) to reduce the polyphase effect. Opaque phases such as large FeNi metal grains relative to the whole chondrule sizes were avoided. Quantitative chemical analyses of lithic fragments and individual silicate phases in chondrules were performed with a focused beam (10 nA) at NIPR, University of Wisconsin-Madison, and Ibaraki University (other analytical settings are the same as those for bulk chondrule analyses). Natural and synthetic standards were chosen based on the compositions of the minerals being analyzed (e.g., Tenner et al., 2015). Detection limits of oxide concentrations are shown in the Supplementary Tables A1.

2.2. Raman spectroscopy

The structural nature of chondrule silica was determined by laser micro-Raman spectroscopy, using a Renishaw inVia spectrometer at NIPR. A microscope was used to focus the excitation laser beam (532 nm). The acquisition time was 30 s. For each region analyzed a Raman spectrum was acquired in the spectral region of 200 to 1400 cm^{-1}.

2.3. Oxygen isotope analyses

Oxygen isotope ratios of non-porphyritic chondrules and lithic fragments in Asuka-881020 were analyzed with the CAMECA IMS-1280 ion microprobe at the WiscSIMS laboratory (Kita et al., 2009). For the oxygen three-isotope analyses, two sizes of focused Cs^+ primary beam (10 × 15 μm at the intensity of ~ 3 nA and 2 × 4 μm at ~ 30 pA) were applied. The analytical conditions and measurement procedures were similar to those in Kita et al. (2010) and Nakashima et al. (2011). The secondary $^{16}O^-$, $^{17}O^-$, and $^{18}O^-$ ions were detected simultaneously by Faraday cups (FCs) and electron multipliers (EMs) on the multicollection system; three FCs for $^{16}O^-$, $^{17}O^-$, and $^{18}O^-$ for 15 μm spot analyses and a FC for $^{16}O^-$ and two EMs for $^{17}O^-$, and $^{18}O^-$ for 4 μm spot analyses. Intensities of $^{16}O^-$ were ~ 3 × 10^9 cps and ~ 2 × 10^7 cps with 15 μm and 4 μm primary beams, respectively. The baselines of the FCs were measured during the presputtering (100 s for 15 μm spots and 360 s for 4 μm spots) in respective analyses and used for data correction. The contribution of the tailing of $^{16}O^1H^-$ interference to $^{17}O^-$ signal was corrected by the method described in Heck et al. (2010), though the contribution was negligibly small (typically < 0.1‰).

One to three analyses were performed for individual chondrules and lithic fragments, bracketed by eight to nine analyses (four or five analyses before and after the unknown sample analyses) on the San Carlos olivine standard grain in a separated mount (Supplementary Table A2). The external reproducibility of the running standard was 0.17 - 0.44‰ for $\delta^{18}O$, 0.34 - 0.66‰ for $\delta^{17}O$, and 0.21 - 0.68‰ for $\Delta^{17}O$ for 15 μm spot analyses, and that for 4 μm spot analyses was 0.81 - 1.18‰ for $\delta^{18}O$, 0.97 - 1.82‰ for $\delta^{17}O$, and 1.09 - 1.98‰ for $\Delta^{17}O$ (2SD; standard deviation). The external reproducibility was assigned as analytical uncertainties of unknown samples (see Kita et al., 2009, 2010 for detailed explanations). We used two olivine (Fo_{100} and Fo_{60}), three low-Ca pyroxene (En_{97}, En_{90}, and En_{85}), diopside, plagioclase (An_{95}), and quartz standards (Valley and Kita, 2009; Kita et al., 2010) in the same sessions for correction of instrumental bias of olivine, pyroxene, plagioclase and silica (Supplementary Table A3). For the CC chondrules which are a sub-μm-sized mixture of low-Ca pyroxene and olivine (Nakashima et

al., 2011), the instrumental biases are calculated based on the volume ratios of olivine to low-Ca pyroxene, Fo#, En#, and Wo# estimated from the EPMA data.

The sample studied was a polished thin section of Asuka-881020 (10 mm × 11 mm) mounted on the center of a 1-inch glass slide. Kita et al. (2009) demonstrated that the instrumental mass fractionation due to stage position is comparable with the reproducibility of the repeated analyses at the center of the SIMS sample holder (~ ±0.3‰ in $\delta^{18}O$; 2SD), if the analysis point is within 6 – 7 mm from the center of the sample holder. Therefore, chondrules and lithic fragments analyzed for oxygen isotopes were searched within 5 mm from the center of the SIMS sample holder. Chondrules and lithic fragments selected for oxygen isotope analysis are larger than the SIMS spot size (> 15 μm). Chondrules composed of multiple mineral phases were analyzed with the 4 μm spots to avoid beam overlap with adjacent mineral phases.

3. Results

Asuka-881020 is mainly composed of non-porphyritic chondrules with a rounded or partially rounded shape, lithic fragments, porphyritic chondrules, and FeNi metal. Fine-grained dark inclusions, similar to those reported in Noguchi et al. (2004), are also observed. The observed non-porphyritic chondrules are classified into CC, SO, and radial pyroxene (RP) chondrules. Among the CC chondrules, there are silica-bearing (SB) and FeNi metal-bearing (MB) chondrules. Furthermore, as described later (Section 3.2), SB chondrules with immiscibility textures are observed, which we call SB-I chondrules. Chemically, the chondrules are classified into FeO-poor (magnesian; Mg# ≥ 90), FeO-rich (ferroan; Mg# < 90), and Al-rich chondrules (Al_2O_3 > 10wt% in bulk composition; Bischoff and Keil, 1984). As described later (Section 3.4), many lithic fragments are mineralogically and chemically similar to the CC chondrules and SB chondrules but have an angular shape. In this paper, we define the objects with ≥ 50% of a rounded outline as the CC and SB chondrules and the objects with < 50% of a rounded outline as CC-like and SB lithic fragments after the definition by Scott (1988).

The non-porphyritic chondrules analyzed for oxygen isotopes include magnesian CC (10), ferroan CC (7), SB (9), MB (4), Al-rich (4), SO (2), and RP (1) chondrules (Fig. 1; Supplementary Fig. A1). Note that proportions of the chondrule types analyzed may not represent their relative abundances in CH chondrites (e.g., Scott, 1988; Ivanova and Petaev, 2015), because our goal was to obtain oxygen isotope data for all major types of non-porphyritic chondrules observed in Asuka-881020.

3.1. CC chondrules

The CC chondrules show a fine-grained/cryptocrystalline texture with longest diameters of 30 – 200 μm (Figs. 1a and 1b; the largest CC chondrule C1 shown in Supplementary Fig. A1). Magnesian cryptocrystalline (MgCC) chondrules have Mg# ranging from 93.9 to 99.4, and ferroan cryptocrystalline (FeCC) chondrules have Mg# ranging from 64.2 to 83.4 (Table 1). The bulk elemental compositions are close to stoichiometric low-Ca pyroxene, though with slight deviations to the high (Mg+Fe)/Si side (Figs. 2a and 2b), suggesting a small contribution of an olivine component (Nakashima et al., 2011; "olivine-pyroxene-normative compositions" in Krot et al., 2010). Two magnesian chondrules have mineralogical and chemical zoning; C5 composed of a low-Ca pyroxene core with tiny Ca-bearing pyroxene grains ($En_{80.2}Wo_{18.8}$) surrounded by a forsterite rim and C8 composed of a slightly Ca-enriched core surrounded by a low-Ca pyroxene rim (detected by SEM-EDS; Supplementary Fig. A1 and Table A1).

3.2. SB and MB chondrules

Nine chondrules, which consist of silica, pyroxene, ± FeNi metal and are surrounded by a Fe-sulfide rim, have a spherical shape with an apparent diameter of 15 – 30 μm (Fig. 1d; Supplementary Fig A1). The chondrules have sharp boundaries between silica and pyroxene, which is textural evidence for formation by liquid immiscibility at high temperatures (> 1968 K; Krot et al., 2000; Hezel et al., 2003; see also Hezel et al., 2006). Pyroxene in the nine SB-I chondrules is low-Ca pyroxene with Wo# < 0.5 and mostly FeO-rich (Mg#: 59.4 – 95.7) (Fig. 2c; Supplementary Table A1), and silica seems to be glassy given the broad Raman peaks.

Four chondrules composed of pyroxene and FeNi metal have a spherical shape with diameters of 15 – 20 μm (Figs. 1g and 1h). The FeNi metal grains are relatively large (8 – 10 μm in size) compared to the whole chondrules. Some CC chondrules contain FeNi metal grains, but which are much smaller than the whole chondrules (≤ 1 μm vs. ~ 100 μm; e.g., C4 in Supplementary Fig A1). Because of the relatively large FeNi metal grains, the four chondrules are classified as MB chondrules. Three of them contain FeNi metal grains with a rounded-to-euhedral shape surrounded by FeO-rich low-Ca pyroxene with Mg# of 66.1 – 75.4. In contrast, in C29, low-Ca pyroxene is FeO-poor (Mg#: 98.3), and the boundary between pyroxene and a FeNi metal grain is not smooth (Fig. 1h).

3.3. Al-rich, SO, and RP chondrules

The Al-rich chondrules have a fine-grained texture composed of pyroxene with Wo# from 13.1 to 26.2 and En# from 73.3 to 86.5, anorthite, ± olivine rim (Figs. 1j and 2d). The Mg# of the Al-rich chondrules range from 89.8 to 99.3 (Table 1).

The SO and RP chondrules have an angular to oval shape with longest diameters of 90 – 200 μm (Fig. 1i; C31 and C32 in Supplementary Fig. A1). The two SO chondrules, which have Mg# of 93.2 and 96.3 (Table 1), consist of olivine, high- and low-Ca pyroxene, and mesostasis. The RP chondrule, which has Mg# of 72.1, consists of a low-Ca pyroxene bar with thickness of 5 – 10 μm and glassy mesostasis.

3.4. Lithic fragments

The lithic fragments are classified into four types; CC-like, SB, olivine, and pyroxene (Figs. 1c, 1f, 1k, and 1l). The CC-like lithic fragments have chemical compositions close to stoichiometric low-Ca pyroxene, slightly deviating towards high (Mg+Fe)/Si, maybe due to a small contribution of an olivine component (Fig. 2e). The olivine-pyroxene-normative compositions are also characteristic for the CC chondrules (Fig. 2a). The low (Mg+Fe)/Si ratio for a MgCC-like lithic fragment (Fig. 2e; F15 in Supplementary Fig. A1), which has the highest Wo# of 8.9 among the MgCC-like lithic fragments, may be due to a contribution of a high-Ca pyroxene component. The CC-like lithic fragments analyzed for oxygen isotopes consist of 33 MgCC-like (Mg#: 91.7 – 99.6) and 2 FeCC-like (Mg#: 77.2 and 86.3) lithic fragments (Table 2).

One of the five SB lithic fragments shows an immiscibility texture between silica and low-Ca pyroxene with Mg# of ~ 60 (F40; Fig. 1c), which is called as SB-I lithic fragment. The other four show no immiscibility texture but instead contain cristobalite, which is identified from 420 and 230 cm^{-1} peaks by Raman spectroscopy. The silicate portion that occurs along with silica in the four SB lithic fragments is pyroxene with variable Wo# from 3.0 to 52.8 (En#: 42.6 – 92.8; Fig. 2c; Supplementary Table A1). One of the four SB lithic fragments consists of low-Ca and high-Ca pyroxene, cristobalite, and microcrystalline mesostasis (F36; Fig. 1f), which is very similar to a cristobalite-bearing chondrule from a CH chondrite (Nakashima et al., 2011) and a

silica-bearing chondrule in a CR chondrite (Krot et al., 2004).

Lithic fragments classified as olivine and low-Ca pyroxene have chemical compositions close to stoichiometric olivine and low-Ca pyroxene respectively. Since oxygen isotope ratios of CC-like and SB(-I) lithic fragments were analyzed in this study, hereafter we focus only on these lithic fragments. The detailed descriptions of olivine and pyroxene fragments will be reported in a separated paper.

3.5. Oxygen isotope ratios

We made a total of 98 spot analyses in 37 chondrules and 40 lithic fragments. After inspection of the SIMS analysis spots by SEM, one analysis was rejected because it overlapped with a crack in a SB lithic fragment (spot 1 in F38; Supplementary Fig. A1). A summary of the 97 spot analyses taken from the 37 chondrules and 40 lithic fragments is shown in Tables 1 – 2; a more complete table is given in the Supplementary Table A2. For CC chondrules and CC-like lithic fragments, one spot analysis was made in the individual objects with the 15 μm beam, because multiple spot analyses showed that oxygen isotope ratios in CC chondrules are internally homogeneous (Nakashima et al., 2011). For other chondrules and lithic fragments composed of multiple mineral phases, one to three spot analyses were made depending on availability of surface area larger than the 4 μm beam.

Oxygen isotope ratios of individual spot analyses in chondrules and lithic fragments show a wide variation from –34‰ to +16‰ in $\delta^{18}O$ along the Primitive Chondrule Mineral (PCM) line (Ushikubo et al., 2012) and between the Carbonaceous Chondrite Anhydrous Mineral (CCAM) and Young and Russell (Y&R) lines (Clayton et al., 1977; Young and Russell, 1998), though most data distribute at $\delta^{18}O > -10$‰ (Fig. 3). The regression line of the oxygen isotope data is $\delta^{17}O = (1.01 \pm 0.02) \times \delta^{18}O - (2.60 \pm 0.17)$ (95% confidence; correlation coefficient = 0.996), which is consistent with the PCM line within the uncertainty (Ushikubo et al., 2012).

Oxygen isotope ratios of the CC chondrules show a variation from –7‰ to +9‰ in $\delta^{18}O$ (Fig. 4a). The isotope data from most MgCC chondrules distribute below the terrestrial fractionation (TF) line and cluster at ~ 0‰ in $\delta^{18}O$. Those from the FeCC chondrules distribute above the TF line with clustering at ~ +7‰ in $\delta^{18}O$. Thus, the FeCC chondrules tend to be ^{16}O-depleted compared to MgCC chondrules. A similar trend is observed for the CC-like lithic fragments. The isotope data from most MgCC-like lithic fragments distribute below the TF line and cluster at ~ 0‰ in $\delta^{18}O$, and those of FeCC-like lithic fragments distribute above the TF line with $\delta^{18}O$ of ~ +6.7‰ (Fig. 4b).

In order to evaluate the homogeneity of oxygen isotope ratios in individual objects (non-porphyritic chondrules and lithic fragments), oxygen isotope ratios between pyroxene (or anorthite) and coexisting mineral phases are compared (Fig. 5). In most cases, the $\delta^{18}O$ values and $\Delta^{17}O$ values of co-existing minerals plot along the 1:1 line within the uncertainty, respectively, indicating that the oxygen isotope ratios in the objects are internally identical. In the two SB-I chondrules (C19 and C22), silica has higher $\delta^{18}O$ values than low-Ca pyroxene exceeding the uncertainty, while their $\Delta^{17}O$ values are indistinguishable (Fig. 5; Table 1). The

oxygen isotopes in silica and low-Ca pyroxene are fractionated in a mass dependent manner, which is discussed later (Section 4.1). The average oxygen isotope ratios of individual objects (SB-I, MB, Al-rich, SO, and RP chondrules and SB and SB-I lithic fragments) are plotted on oxygen three-isotope diagrams (Figs. 4c and 4d). The uncertainties of the average values in the individual objects were estimated from twice the standard error of the mean (2SE) of multiple data (n), unless it is smaller than the weighted average of data (2SE = 2SD of bracketing standard analyses divided by the square root of n). As shown in Fig. 4c, the isotope ratios that plot above the TF line with clustering at ~ +7‰ in $\delta^{18}O$ are from FeO-rich MB and SB-I chondrules and the SB-I lithic fragment. The SB lithic fragments, of which Mg# is variable from 82.5 to 94.9, show a variation from –5‰ to +15‰ in $\delta^{18}O$. The FeO-poor MB chondrule (C29) has ^{16}O-rich isotope ratios with $\delta^{18}O$ of ~ –34‰ (Table 1; see also Fig. 3). One of the Al-rich chondrules is FeO-rich and the isotope ratios plot above the TF line with $\delta^{18}O$ of ~ +7‰ (Fig. 4d; Table 1). Other three Al-rich chondrules, which are FeO-poor, plot below the TF line. The FeO-poor SO and FeO-rich RP chondrules distribute below the TF line with $\delta^{18}O$ of ~ 0‰ and +2.5‰, respectively (Fig. 4d).

To summarize, the oxygen isotope data from most FeO-poor objects are distributed below the TF line and those from most FeO-rich objects distribute above the TF line, indicating that FeO-poor objects tend to have more ^{16}O-rich compositions than the FeO-rich objects. This trend is evident in Fig. 6a (including data from previous studies), where the $\Delta^{17}O$ values of non-porphyritic chondrules and lithic fragments are plotted versus their Mg#. The FeO-poor objects have Mg# of 91 – 99 and negative $\Delta^{17}O$ values, and the FeO-rich objects have Mg# of 55 – 89 and positive $\Delta^{17}O$ values; there are some exceptions.

4. Discussion

4.1. Classification of non-porphyritic chondrules and lithic fragments based on the $\Delta^{17}O$ values and Mg#

In the previous studies, oxygen isotope analyses of non-porphyritic chondrules in CH and CB chondrites were obtained mostly from MgCC chondrules, which are very abundant in these chondrites (e.g., Scott, 1988) and show indistinguishable $\Delta^{17}O$ values of ~ –2.2‰ (Krot et al., 2010; Nakashima et al., 2011). In this study, other types of objects, such as non-porphyritic chondrules and lithic fragments, with the full range of Mg# and various textures are analyzed for oxygen isotopes. Figure 6a compares Mg# and $\Delta^{17}O$ values of the measured objects (non-porphyritic chondrules and lithic fragments) in Asuka-881020 and other CH and CB chondrites (n = 140; Krot et al., 2001b, 2010, 2012; Kobayashi et al., 2003; Nakashima et al., 2011). While the $\Delta^{17}O$ values and Mg# are highly variable from ~ –21‰ to ~ +5.1‰ and from ~ 60 to ~ 99, about 50% of the measured objects have $\Delta^{17}O$ values of ~ –2‰ and Mg# higher than 98 (Figs. 6b and c). There are two additional small peaks around +1.5‰ for FeO-rich objects with Mg# of ~ 55 – 89 and around –6‰ for FeO-poor objects with Mg# of ~ 91 – 99 (Figs. 6a and c). Hereafter the objects with $\Delta^{17}O$ of ~ –6‰, –2‰, and +1.5‰ are called as the –6.3‰

group, the –2.3‰ group, and the +1.4‰ group according to the average $\Delta^{17}O$ values of individual group objects, which are described in detail later. The objects that are not classified into one of the three groups are called as "others".

Ninety-one objects have nearly identical $\Delta^{17}O$ values with an average of –2.3 ± 0.7‰ (2SD) and are classified into the –2.3‰ group, which comprises 65% of the measured objects. The Mg# of these objects range from 91.7 to 99.6 (Fig. 6a). The –2.3‰ group is composed of MgCC and SO chondrules and MgCC-like lithic fragments (Table 3). Since the MgCC chondrules and MgCC-like lithic fragments share common properties of olivine-pyroxene-normative compositions (Figs. 2a and 2e), depletion in refractory elements with variable degrees (Fig. 7a), and $\Delta^{17}O$ values of ~ –2.3‰, it is likely that the MgCC-like lithic fragments are fragments of MgCC chondrules, as suggested in Scott (1988) and Weisberg et al. (1988). Hereafter the MgCC-like lithic fragments are called as MgCC chondrule fragments. The fragmentation may have occurred during accretion onto the parent body and/or brecciation on the surface of the parent body. The latter case is possible if Asuka-881020 is a breccia.

Twenty-six objects have positive $\Delta^{17}O$ values with an average of +1.4 ± 1.2‰ (2SD) and are classified into the +1.4‰ group, which comprises 19% of the measured objects. The Mg# range from 58.5 to 95.4 (Fig. 6a). This group is composed of FeCC, MgCC, SB-I, FeO-rich MB, and FeO-Al-rich chondrules and FeCC-like lithic fragments (Table 3). It is likely that the FeCC-like lithic fragments are fragments of FeCC chondrules, given the common properties of the positive $\Delta^{17}O$ values, FeO-rich olivine-pyroxene-normative compositions (Figs. 2b and 2e), and depletion in refractory elements (Fig. 7b). Therefore, the FeCC-like lithic fragments are called as FeCC chondrule fragments. Krot et al. (2014) reported that FeCC chondrules have a variation in $\Delta^{17}O$ values from ~ –2‰ to +2‰, but the FeO-rich objects analyzed in this study have positive $\Delta^{17}O$ values, except for the FeO-rich RP chondrule (C32) with –1.1‰ and the SB lithic fragment (F38) with –3.9‰.

In the two SB-I chondrules (C19 and C22) that belong to the 1.4‰ group, silica and low-Ca pyroxene show a mass dependent oxygen isotope fractionation (Fig. 5), which might be due to oxygen isotope exchange with fluid having a similar $\Delta^{17}O$ value to those of the two chondrules during aqueous alteration in the parent body, as CH chondrites contain phyllosilicate around chondrules and glass clasts (Krot et al., 2000; Greshake et al., 2002; Noguchi et al., 2004, 2005). Although the $\Delta^{17}O$ value of water in CH chondrites is unknown, water in CR chondrites, which are genetically related to CH chondrites (Krot et al., 2002), has a $\Delta^{17}O$ value ranging from –1.2‰ to +1‰ (Jilly-Rehak et al., 2018), which is consistent with those of the two chondrules within the uncertainty. Under wet conditions, diffusion of oxygen in quartz is faster than that in diopside, though the temperature ranges (900 – 1100 K for quartz and 1000 – 1500 K for diopside; Farver, 2010) are higher than that for aqueous alteration in chondrite parent bodies (270 – 600 K; Brearley, 2006). Because the oxygen isotope ratios of silica in the two chondrules do not reflect the final chondrule formation event, these are not used for further discussion.

Ten objects have nearly identical $\Delta^{17}O$ values with an average of –6.3 ± 0.7‰ (2SD) and are classified into the –6.3‰ group, which comprises 7% of the measured objects. The Al-rich,

MgCC, and SB chondrules and SB lithic fragment comprising this group show a range of Mg# from 91.1 to 99.3 (Table 3; Fig. 6a).

Thirteen objects, which include MgCC, FeO-poor MB, Al-rich, and RP chondrules and MgCC-like and SB lithic fragments, have variable $\Delta^{17}O$ values ranging from –20.6‰ to +5.1‰ and Mg# from 82.5 to 99.4 (Fig. 6a; Table 3). They are classified as "others". Their $\Delta^{17}O$ values are different (or marginally different) from those of the three groups, and the chemical compositions cannot be explained by the formation along with the three group objects (see section 4.4).

Thus, the non-porphyritic chondrules and lithic fragments are classified into three groups with distinct $\Delta^{17}O$ values and Mg#, and at least three distinct environments and/or formation histories are required to form the non-porphyritic chondrules in CH and CB chondrites. It is important to note that (1) MgCC chondrules and MgCC chondrule fragments are observed in all three groups and "others", (2) SO chondrules are only observed in the –2.3‰ group, (3) SB objects are not observed in the –2.3‰ group, and (4) most objects with positive $\Delta^{17}O$ values have FeO-rich compositions (Table 3). These observations are essential for understanding the formation processes and environments of the non-porphyritic chondrules in CH and CB chondrites, which are discussed in section 4.3.

4.2. Comparison of $\Delta^{17}O$-Mg# trend for non-porphyritic chondrules and lithic fragments in CH and CB chondrites with those for chondrules in other carbonaceous chondrites

Overall, the $\Delta^{17}O$ values of the measured objects in CH an CB chondrites increase with decreasing Mg# (Fig. 6a). Similar $\Delta^{17}O$-Mg# trends are observed for the chondrules in other carbonaceous chondrites (Fig. 8; Connolly and Huss, 2010; Russell et al., 2010; Ushikubo et al., 2012; Tenner et al., 2013, 2015, 2017, 2018; Schrader et al., 2013, 2014, 2017; Chaumard et al., 2018; Hertwig et al., 2018, 2019a, 2019b; Yamanobe et al., 2018). Here we compare the oxygen isotope systematics of the measured objects in CH and CB chondrites with those of chondrules in other carbonaceous chondrites.

For Acfer 094 and Yamato-81020 (CO3.0), there is mainly a bimodal distribution of $\Delta^{17}O$ at ~ –5‰ and ~ –2‰ for chondrules with Mg# > 97 and < 97 (including type II chondrules), respectively (Fig. 8a; Ushikubo et al., 2012; Tenner et al., 2013; Hertwig et al., 2019a). Similar results are observed from Yamato-82094 (ungrouped C3.2), Kaba (CV3), Northwest Africa (NWA) 8613 (CV3), Murchison (CM), and Northwest Africa 5958 (CM-related), though the chondrules with $\Delta^{17}O$ of ~ –5‰ have tightly clustered Mg# at ~ 99 and a limited number of chondrules have $\Delta^{17}O$ values of ≥ –2‰ and lower Mg# (Tenner et al., 2017; Chaumard et al., 2018; Hertwig et al., 2018, 2019b; Marrocchi et al., 2018, 2019). Chondrules in CR chondrites show a different $\Delta^{17}O$-Mg# trend (Fig. 8b). The $\Delta^{17}O$ values of most type I chondrules (Mg# ≥ 90) cluster at –2‰ with most Mg-rich chondrules (Mg# ≥ 98) being systematically lower in $\Delta^{17}O$ down to –5‰ (Tenner et al., 2015), while those of type II chondrules vary from –2‰ to +1‰ (Connolly and Huss, 2010; see also Schrader et al., 2013, 2014, 2017). The $\Delta^{17}O$-Mg# trend of chondrules and chondrule fragments in the Tagish Lake-type carbonaceous chondrites is similar

to that of the CR chondrite chondrules, but different in lacking in type I chondrules with Mg# < 98 and $\Delta^{17}O \sim -2‰$ (Russell et al., 2010; Yamanobe et al., 2018). Thus, the oxygen isotope systematics are specific to the individual carbonaceous chondrite groups.

It was pointed out that Mg-rich chondrules with $\Delta^{17}O$ of ~ –5‰ are commonly observed in multiple carbonaceous chondrites (e.g., Tenner et al., 2017, 2018). They suggested that many carbonaceous chondrites sampled precursors from a common oxygen isotope reservoir, even though chondrules in each group of carbonaceous chondrites would have formed in separated regions in the protoplanetary disk at different timing (Jones, 2012; Hezel and Parteli, 2018; Hezel et al., 2018). Furthermore, the negative $\Delta^{17}O$-Mg# correlations are common to all the carbonaceous chondrites, which are explained by an addition of ^{16}O-poor water ice as an oxidant to the relatively ^{16}O-rich anhydrous solid precursors (e.g., Tenner et al., 2015; Hertwig et al., 2018). As a ^{16}O-poor counterpart, SiO-rich gas was also suggested (e.g., Marrocchi and Chaussidon, 2015).

For non-porphyritic chondrules and lithic fragments in CH and CB chondrites, the objects that belong to the –2.3‰ group (the most abundant group) are FeO-poor (Mg# = 91.7 – 99.6) and have nearly identical $\Delta^{17}O$ values with an average of –2.3 ± 0.7‰ (Fig. 6a). The +1.4‰ group objects are relatively FeO-rich (Mg# = 58.5 – 95.4) and have positive $\Delta^{17}O$ values with an average of +1.4 ± 1.2‰. The –6.3‰ group objects are FeO-poor (Mg# = 91.1 – 99.3) and have lower $\Delta^{17}O$ values with an average of –6.3 ± 0.7‰. The $\Delta^{17}O$-Mg# trend is different from those of chondrules in other chondrite groups, though the distribution of $\Delta^{17}O$ is somewhat similar to that of CR chondrite chondrules (Figs. 6a and 8). This is consistent with common characteristics for CH, CB, and CR chondrites (CR chondrite clan; Krot et al., 2002); relatively high modal abundances of FeNi metal compared to other carbonaceous chondrites (> 5 vol%), isotopically heavy nitrogen in bulk meteorites ($\delta^{15}N \sim +200$ to +1000‰), and similar oxygen isotope ratios of whole rocks (e.g., Weisberg et al., 1995; Krot et al., 2002; Scott and Krot, 2003).

However, it should be noted that there are notable differences between chondrules in CH and CR chondrites. Chondrule sizes in CH chondrites are much smaller than that in CR chondrites (~ 20 μm vs. ~ 700 μm; Friedrich et al., 2014). More than 80% of chondrules in CH chondrites are non-porphyritic and chemically fractionated types, while more than 96% of chondrules in CR chondrites are a porphyritic type (Scott and Krot, 2003). Furthermore, if comparing the $\Delta^{17}O$-Mg# trend for the FeO-poor objects in CH and CB chondrites with that for the type-I chondrules in CR chondrites (Figs. 6a and 8), there is no systematic difference in Mg# between the –2.3‰ and –6.3‰ groups, while the CR chondrules with $\Delta^{17}O$ of ~ –2‰ have lower Mg# than those with $\Delta^{17}O$ of ~ –5‰. Thus, the origin of the –2.3‰ and –6.3‰ groups in CH and CB chondrites would require a scenario that would be very different from the mixing model of Tenner et al. (2015) for CR chondrite chondrules involving ^{16}O-rich anhydrous precursors and ^{16}O-poor water ice.

4.3. Formation processes of the non-porphyritic chondrules in CH and CB chondrites

4.3.1. Formation processes of non-porphyritic chondrules with $\Delta^{17}O$ of ~ –2.3‰

Most chondrules in CH and CB chondrites are non-porphyritic types such as CC and SO chondrules with FeO-poor compositions (e.g., Krot et al., 2001a, 2010). While the CC chondrules are depleted in refractory elements such as Ca, Al, and Ti, the SO chondrules are enriched in refractory elements (Krot et al., 2001a). Regardless of the differences in textures and chemistry, the CC and SO chondrules have nearly identical $\Delta^{17}O$ values; –2.2 ± 0.5‰ for CC chondrules (average ± 2SD; Krot et al., 2010; see also Nakashima et al., 2011) and –2.4 ± 1.3‰ for SO chondrules (Krot and Nagashima, 2017; not plotted in Fig. 6a). It has been suggested that the CC and SO chondrules formed via fractional condensation from an isotopically uniform gaseous reservoir with $\Delta^{17}O$ of ~ –2.2‰ generated by a single-stage heating event; a large-scale impact or a highly energetic thermal event in the dusty region of the solar nebula (e.g., Petaev et al., 2001; Krot et al., 2010). The SO chondrules are isolated from the reservoir prior to the condensation of the CC chondrules (Fig. 9a; Petaev and Wood, 1998; Krot and Nagashima, 2017). The formation process suggested in the previous studies is consistent with our new data. The –2.3‰ group is the majority of the measured objects, in which the SO and MgCC chondrules and MgCC chondrule fragments are included (Table 3), and they have nearly identical $\Delta^{17}O$ values of ~ –2.3‰. The SO chondrules are relatively enriched in refractory elements compared to the MgCC chondrules and MgCC chondrule fragments (Fig. 7a).

The variation in Mg# from 91.7 to 99.6 for the MgCC chondrules and MgCC chondrule fragments in Asuka-8801020 is larger than that for the MgCC chondrules in other CH and CB chondrites (94.1 – 99.6; Krot et al., 2010; Nakashima et al., 2011). According to Petaev et al. (2001), the CC chondrules with Mg# of 96 – 99 formed during fractional condensation under an environment with dust/gas ratios of 10 – 50 x solar; chondrules with lower Mg# require higher dust/gas ratios (see also Krot et al., 2001a). Given the MgCC chondrules and MgCC chondrule fragments with Mg# < 96 in Asuka-881020, the chondrule-forming environment with $\Delta^{17}O$ of –2.3‰ may have had variable dust/gas ratios of ~ 10 – 50 x solar and above.

4.3.2. Relationship among the three distinct oxygen isotope groups in CH chondrite chondrules

As discussed in the previous sections, at least three distinct environments and/or formation histories are required to explain the formation of the CH non-porphyritic chondrules, which include not only CC and SO chondrules but also SB, MB, and Al-rich chondrules. The SB chondrules and fragments are occasionally observed in CH chondrites as well as in ordinary chondrites (Brigham et al., 1986; Krot et al., 2000, 2007; Hezel et al., 2003, 2006; Ivanova et al., 2008; Nakashima et al., 2011; Ivanova and Petaev, 2015). The Gujba CB_a chondrite contains coesite and quartz (Weisberg and Kimura, 2010). According to Petaev and Wood (1998), silica can form during fractional condensation of a gas of solar composition with Mg/Si < 1, which is achieved when the isolation degree (ξ; degree of isolation of condensates from the residual gas) is 0.47% or above. Ivanova and Petaev (2015) suggested that the bulk elemental compositions of most chondrules in a CH chondrite are explained by fractional condensation at ξ = 1%. At ξ = 1%, silica condenses at a lower temperature (1215 K) than other silicate phases; diopside (1333 K), olivine (1319 – 1316 K), and low-Ca pyroxene (1268 – 1258 K) (Petaev and Wood, 1998). It is considered that the SB chondrules formed posterior to the SO and CC chondrules during fractional condensation. As we pointed out in the previous section, the SO chondrules are only observed in the –2.3‰ group, and the SB objects are not observed in the –2.3‰ group but in

other groups (Table 3). In the +1.4‰ group, the SB-I chondrules and lithic fragment show immiscibility textures (Figs. 1c and 1d), which require a heating at > 1968 K (Hezel et al., 2003). In the –6.3‰ group, the SB lithic fragment and chondrule contain cristobalite (Fig. 1f; Nakashima et al., 2011), which require a heating at 1743 – 1968 K (Hezel et al., 2003). We infer that the SB(-I) chondrules and fragments experienced reheating events at high temperatures after condensation at ~ 1200 K. The simple interpretation of these observations is that the $\Delta^{17}O$ value of the chondrule-forming environment has been changed from –2.3‰ to +1.4‰ and/or –6.3‰ when reheating events and condensation of silica-normative materials occurred, though the heat sources are unknown. Hereafter this hypothesis is tested based on the mineralogy, chemistry and $\Delta^{17}O$ values of the non-porphyritic chondrules and lithic fragments.

Relationship between the two chondrule groups with $\Delta^{17}O$ of –2.3‰ and –6.3‰

The ^{16}O-depleted igneous CAIs in CH chondrites have $\Delta^{17}O$ values of ~ –6‰ (Krot et al., 2012, 2017a; Fig. 6a) that are similar to those of the –6.3‰ group discussed above. Krot et al. (2012) suggested that the ^{16}O-depleted igneous CAIs resulted from remelting of pre-existing ^{16}O-rich CAIs ($\Delta^{17}O$ ~ –22‰) during formation of CC and SO chondrules in the CH and CB chondrites. The $\Delta^{17}O$ values of ~ –6.3‰ for the chondrules may also be explained by a mixing between the $\Delta^{17}O$ values of ~ –22‰ from the pre-existing CAIs and that of –2.3‰ of the gaseous environment for the SO and MgCC chondrules. Given that the SO chondrules are only observed in the –2.3‰ group and that the SB objects are observed in the –6.3‰ group but not in the –2.3‰ group (Table 3), it is considered that the ^{16}O-rich CAIs were incorporated into the gaseous environment with $\Delta^{17}O$ of –2.3‰ when condensing silica-normative materials after isolation of the SO and MgCC chondrules (Fig. 9a).

The SO chondrule formation occurred ~ 5 Myr after the CAI formation (Krot et al., 2005; Bollard et al., 2015), which postdate the accretion of other chondritic asteroids that would have occurred ~ 2 – 3 Myr after the CAI formation (e.g., Fujiya et al., 2012; Doyle et al., 2015). It is likely that a fraction of ^{16}O-rich refractory solids in the protoplanetary disk might have escaped from accretion to early formed chondritic asteroids and were incorporated into the –2.3‰ environment of the CH chondrite forming regions. They might have been similar to CAIs and/or amoeboid olivine aggregates (AOAs), but could have been surrounded by unfractionated fine-grained dust (Scott and Krot, 2005).

It is expected that the refractory element abundances of the –6.3‰ group objects decrease with the order of Al-rich, MgCC, and SB chondrules, if they formed via fractional condensation. However, the SB chondrule and fragment are enriched in refractory elements relative to the MgCC chondrules and even those in the –2.3‰ group (Figs. 7a, 7c, and 7e). This may be explained by remelting of the silica-normative materials that condensed on the ^{16}O-rich refractory solids, as the presence of cristobalite requires reheating after condensation of silica-normative materials. The Al-rich chondrules of the –6.3‰ group may also be remelting products of the ^{16}O-rich refractory solids. The Al-rich chondrules are surrounded by olivine rims (Supplementary Fig. A1), suggesting the preferential loss of Si relative to Mg during melt evaporation (Krot et al., 2012) and/or condensation of Mg into the chondrule melts (Krot et al., 2017a). Similarly, the MgCC chondrule (C5) has the olivine rim (Supplementary Fig. A1),

though the chondrule is not refractory-rich. The chondrule may have acquired oxygen isotopes with $\Delta^{17}O$ of ~ –6‰ by equilibrating with the surrounding gas of which $\Delta^{17}O$ value changed from –2.3‰ to –6.3‰ during the reheating event. Thus, mineralogy, chemistry, and $\Delta^{17}O$ values of the chondrules in the –2.3‰ and –6.3‰ group do not contradict with the hypothesis that the $\Delta^{17}O$ value of the chondrule-forming environment changed from –2.3‰ to –6.3‰.

Krot et al. (2017b) observed relict CAIs within porphyritic chondrules in CH chondrites, which have variable $\Delta^{17}O$ values ranging from –37‰ to +4‰. The –6.3‰ group objects may possibly be complete melt products of such compound objects. However, the refractory element abundances of the –6.3‰ group objects (except for Al-rich chondrules; Fig. 7c) cannot be explained by the mixing between CAIs and porphyritic chondrules with refractory element abundances of ~ 1 × CI (Grossman et al., 1988; Scott, 1988).

Relationship between the two chondrule groups with $\Delta^{17}O$ of –2.3‰ and +1.4‰

The +1.4‰ group has FeO-rich compositions and higher $\Delta^{17}O$ values than the other two groups (Fig. 6a). This may be explained by an addition of ^{16}O-poor water ice to a relatively ^{16}O-rich solids, as in the case of chondrules in other carbonaceous chondrites (e.g., Tenner et al., 2015). The $\Delta^{17}O$ value of the relatively ^{16}O-rich solids may be –2.3‰. As a ^{16}O-poor counterpart, SiO-rich gas may also be possible, which produces pyroxene via a high-temperature reaction with precursor olivine (e.g., Marrocchi and Chaussidon, 2015). Pyroxene shows variable $\delta^{18}O$ values depending the $\delta^{18}O$ values of precursor olivine and dust/gas ratios, though with steeper slopes of the $\delta^{17}O$ - $\delta^{18}O$ correlation lines than the PCM line; e.g., slope of 1.44 at $\delta^{18}O_{olivine}$ = 0‰ with dust/gas ratios from 0 to 200. Pyroxene with ^{16}O-poor isotope ratios seems to distribute on the left side of the PCM line (i.e., lower $\delta^{18}O$ side), unlike the FeCC chondrules of which oxygen isotope data distribute along the PCM line (Fig. 4a). Therefore, the SiO-rich gas is unlikely to be the ^{16}O-poor counterpart.

If changing the $\Delta^{17}O$ value from –2.3‰ to +1.4‰ and the redox condition from reducing to oxidizing in the chondrule-forming environment, ^{16}O-poor water ice should have been added and evaporated. Given that the SO chondrules are only observed in the –2.3‰ group and that the SB-I chondrules are only observed in the +1.4‰ group (Table 3), the timing of the $\Delta^{17}O$ change could be when condensing silica-normative materials after isolation of SO and MgCC chondrules. If this is the case, it is expected that the +1.4‰ group objects are highly depleted in refractory elements compared to the SO and MgCC chondrules. But, the +1.4‰ group objects show large variations in refractory element abundances from < 0.01 × CI to ~ 4 × CI, which are comparable to those of the –2.3‰ group objects (Figs. 7a, 7b, and 7e). Instead of the hypothesis that the $\Delta^{17}O$ value of the chondrule-forming environment changed from –2.3‰ to +1.4‰, it is inferred that the two chondrule-forming environments existed in the separated regions, from which non-porphyritic chondrules formed via fractional condensation. Given the presence of the four objects (C10, F11, F23, and F27) with intermediate $\Delta^{17}O$ values between –2.3‰ and +1.4‰ (Fig. 6a; classified as “others”), the intermediate chondrule-forming environment may have

existed.

The refractory element abundances of the +1.4‰ group objects decrease with the order of ferroan Al-rich, FeCC (including fragment), MgCC, ferroan MB, and SB-I chondrules, which is consistent with the order expected from fractional condensation (Petaev and Wood, 1998). Since Fe-sulfide rims occur only around the SB-I chondrules (maybe troilite; e.g., Figs. 1d and 1e), the SB-I chondrules may have remained in the chondrule-forming environment after isolation of other types of chondrules and even after reheating until condensation of Fe-sulfide (Fig. 9b; ~ 730 – 750 K at $\xi \leq 2\%$; Petaev and Wood, 1998).

4.3.3. Summary and possible heat sources of the multiple chondrule-forming events

So far, we discussed relationships among the three groups with distinct $\Delta^{17}O$ values and suggested that multiple chondrule-forming environments and heating events are required for the non-porphyritic chondrules in CH and CB chondrites. The $\Delta^{17}O$ value of the chondrule-forming environment may have changed from –2.3‰ to –6.3‰ due to an addition of ^{16}O-rich refractory solids and a reheating event when condensing silica-normative materials after isolation of the SO and MgCC chondrules (Fig. 9a). The environment with $\Delta^{17}O$ of +1.4‰ may have separately existed, from which various types of chondrules formed via fractional condensation and a reheating event (Fig. 9b). It should be noted that the reheating events (drawn in gray in Fig. 9) would have been localized and did not affect all the chondrules and fragments. It is worth mentioning that CH chondrites contain zoned CC chondrules composed of a FeO-poor core and a FeO-rich rim (Ivanova et al., 2008; Krot et al., 2014; Ivanova and Petaev, 2015). Ivanova and Petaev (2015) suggested that the zoned CC chondrules formed through a multi-stage process; formation of a FeO-poor core in a reducing environment followed by formation of a FeO-rich rim in an oxidizing environment. If this is the case, it is inferred that formation of the +1.4‰ objects occurred after that of the –2.3‰ objects. The evolution path of the $\Delta^{17}O$ values and Mg# is different from that for the chondrules in other carbonaceous chondrites; $\Delta^{17}O$ values and Mg# evolve in one direction from relatively ^{16}O-rich and FeO-poor to ^{16}O-poor and FeO-rich (Fig. 8; e.g., Tenner et al., 2015; Hertwig et al., 2018), though the negative $\Delta^{17}O$-Mg# correlations are commonly observed for the chondrules in all the carbonaceous chondrites.

It has been suggested that CC and SO chondrules formed via fractional condensation in an isotopically uniform gaseous environment generated by a single-stage heating event (e.g., Krot et al., 2010). There are two possible heat sources; a large-scale impact and a highly energetic thermal event in the solar nebula (e.g., Petaev et al., 2001; Krot et al., 2005, 2010). The former is based on the argument that the protoplanetary disk has been largely dissipated when the SO chondrules formed (~ 5 Myr after the CAI formation; e.g., Krot et al., 2005; Hartmann, 2005; Hernández et al., 2007). The latter is based on the argument that high concentrations of H_2 in FeNi metal in a CB chondrite ($\geq$ 28 ppm) requires condensation of FeNi metal and non-porphyritic chondrules in a pressure-enhanced region of the solar nebula (Lauretta et al., 2005; see also Petaev et al., 2006). Although it is not clear which heat source is likely, the –2.3‰ group objects may have formed in an isotopically uniform gaseous environment generated by the single-stage heating event. However, the single-stage heating event cannot be responsible for all the non-porphyritic chondrules with variable $\Delta^{17}O$ values, Mg#, and textures, as discussed so far.

Instead, multiple chondrule-forming environments and heating events are required. The +1.4‰ group objects may have formed via fractional condensation in a gaseous environment with $\Delta^{17}O$ of +1.4‰ generated by the same heat source as that for the –2.3‰ group objects. Furthermore, reheating events are required for the formation of the –6.3‰ group objects and SB-I chondrules with $\Delta^{17}O$ of ~ +1.4‰. In either heat source (large-scale impact or highly energetic thermal event in the solar nebula), multiple heating events and environments are required for the formation of the non-porphyritic chondrules in CH chondrites.

It should be noted that non-porphyritic chondrules in CB chondrites are mostly SO and MgCC chondrules, which are explained by the formation from the gaseous environment with $\Delta^{17}O$ of –2.2‰ generated by the single-stage heating event (Krot et al., 2010; Krot and Nagashima, 2017). FeCC, SB, MB, and MgCC chondrules with distinct $\Delta^{17}O$ values are apparently absent in CB chondrites. Therefore, it appears that non-porphyritic chondrules in CB chondrites may not require multiple chondrule-forming environments and chondrule heating events in contrast to those in CH chondrites. Furthermore, the non-porphyritic chondrules are larger than those in CH chondrites (Scott and Krot, 2003). Thus, non-porphyritic chondrules in CH chondrites and those in CB chondrites share common properties but have differences.

4.4. Chondrules and lithic fragments with distinct $\Delta^{17}O$ values

In the measured objects in CH and CB chondrites, more than 90% are explained by the formation from the three distinct environments with $\Delta^{17}O$ of –6.3‰, –2.3‰, and +1.4‰, including the four objects of which $\Delta^{17}O$ values are intermediate between –2.3‰ and +1.4‰. Remaining nine objects, which are called “others”, may have different origins. They may have formed along with type-I and -II porphyritic chondrules in CH and CB chondrites, which have variable $\Delta^{17}O$ values ranging from ~ –5‰ to ~ +5‰, respectively (Krot et al., 2010).

Among the three SB lithic fragments, F37 has Mg# of 95.1 and marginally lower $\Delta^{17}O$ value of –3.4 ± 0.2‰ than those of the –2.3‰ group (–2.3 ± 0.7‰; Fig. 6a). But, condensation of the fragment in the –2.3‰ environment after isolation of the MgCC chondrules is unlikely, as the refractory element abundances are not lower than those in the MgCC chondrules (Figs. 7a and 7d). Other two (F38 and F39) have Mg# of 86.6 and 82.5 and different $\Delta^{17}O$ values of –3.9 ± 2.0‰ and +5.2 ± 1.0‰ from those of the +1.4‰ group (+1.4 ± 1.2‰). The relatively high refractory element abundances compared to the FeCC chondrules cannot be explained by condensation after isolation of the FeCC chondrules (Figs. 7b and 7d). It may be possible that the three SB lithic fragments formed along with the porphyritic chondrules in the CH and CB chondrites. The same may be true for the MgCC chondrule with $\Delta^{17}O$ of +2.2 ± 0.1‰ (Ch01; Figs. 6a and 7d; Nakashima et al., 2011), which cannot be explained by the formation from the –2.3‰ environment. The ferroan RP chondrule (C32), of which $\Delta^{17}O$ value is –1.1 ± 0.3‰, could have formed along with the type-II porphyritic chondrules.

The $\Delta^{17}O$ values of ~ –10‰ from an Al-rich chondrule (C37) and two MgCC-like lithic fragments (F24 and F29; Fig. 6a) are outside of the $\Delta^{17}O$ range of the type-I and -II porphyritic

chondrules (Krot et al., 2010), suggesting formation from a distinct environment. The FeO-poor MB chondrule (C29) has the $\Delta^{17}O$ value of ~ –21‰, which is within the $\Delta^{17}O$ range of ^{16}O-rich CAIs in CH chondrites (–22.2 ± 3.6‰; Krot et al., 2012). But, the refractory element abundances in the chondrule are not as high as those in Al-rich chondrules (Fig. 7) and CAIs (> 1 × CI; Krot et al., 2001b; Ivanova and Petaev, 2015). As in the case of the extremely ^{16}O-rich chondrule in Acfer 214 (a006; Kobayashi et al., 2003), the FeO-poor MB chondrule may have formed from a ^{16}O-rich environment or preserved the ^{16}O-rich isotope ratios after melting.

5. Conclusions

Oxygen isotope ratios and major elemental compositions of non-porphyritic chondrules and lithic fragments in the Asuka-881020 CH chondrite were measured to investigate oxygen isotope systematics of the non-porphyritic chondrules in CH and CB chondrites. The chondrules exhibit textural variation; cryptocrystalline ± silica ± FeNi metal, skeletal olivine (SO), and radial pyroxene. The Al-rich chondrules are also observed. The oxygen isotope ratios plot along the primitive chondrule mineral line with $\Delta^{17}O$ values from ~ –21‰ to ~ +5‰, and three groups in $\Delta^{17}O$ values (+1.4‰, –2.3‰, and –6.3‰) are recognized. The $\Delta^{17}O$ values increase with decreasing Mg# from 99.6 to 55.3, similarly to the $\Delta^{17}O$-Mg# trends for the chondrules in other carbonaceous chondrites. The –2.3‰ group, which has indistinguishable $\Delta^{17}O$ values with an average of –2.3 ± 0.7‰ and Mg# ranging from 91.7 to 99.6, is composed of SO and magnesian cryptocrystalline (MgCC) chondrules and MgCC chondrule fragments. The +1.4‰ group, which has positive $\Delta^{17}O$ values with an average of +1.4 ± 1.2‰ and Mg# ranging from 58.5 to 95.4, is composed of FeO-Al-rich, ferroan cryptocrystalline (FeCC), metal-bearing FeO-rich, and silica-bearing (SB) chondrules with immiscible textures and FeCC chondrule fragments. The –6.3‰ group, which has $\Delta^{17}O$ values with an average of –6.3 ± 0.7‰ and Mg# ranging from 91.1 to 99.3, is composed of Al-rich, MgCC, and SB chondrules and SB lithic fragment.

Given the absence of the SB objects in the –2.3‰ group, it is suggested that the $\Delta^{17}O$ value of the chondrule-forming environment has been changed from –2.3‰ to –6.3‰ and/or +1.4‰ when condensing the silica-normative materials. Since the variations in the refractory element abundances in the +1.4‰ group objects are as large as those in the –2.3‰ group objects, the change of $\Delta^{17}O$ value from –2.3‰ to +1.4‰ is unlikely. The chondrule-forming environment with $\Delta^{17}O$ of +1.4‰ that was produced by the addition and evaporation of ^{16}O-poor water ice may have existed separately, from which chondrules formed via fractional condensation and a reheating event. The change of $\Delta^{17}O$ value from –2.3‰ to –6.3‰ due to an addition of ^{16}O-rich refractory solids with $\Delta^{17}O$ of ~ –22‰ followed by a reheating event can explain the SB objects that are relatively enriched in refractory elements compared to the MgCC chondrules. The Al-rich chondrules with $\Delta^{17}O$ of ~ –6.3‰ are likely to be products during the reheating event. Chondrules and lithic fragments that are not classified into the three groups may have formed in distinct environments. Thus, multiple chondrule-forming environments and heating events are required to form the non-porphyritic chondrules in CH and CB chondrites.

Acknowledgements

The authors thank NIPR for use of Asuka-881020 thin section for this study, J. Kern and T.J. Tenner for SIMS support, J. Fournelle for EPMA support, and Sasha Krot for kindly providing oxygen isotope data of SO chondrules in metal-rich carbonaceous chondrites and handling of the manuscript. A. Yamaguchi helped to conduct EPMA and Raman analyses at NIPR. Reviews of D.C. Hezel and two anonymous reviewers significantly improved the manuscript. This work was supported by the NASA Cosmochemistry program (NNX11AG62G). WiscSIMS is partly supported by NSF (EAR10-53466, EAR-1658823).

References

Anders E. and Grevesse N. (1989) Abundances of the elements: Meteoritic and solar. *Geochim. Cosmochim. Acta* **53**, 197–214.

Baertschi P. (1976) Absolute ^{18}O content of standard mean ocean water. *Earth Planet. Sci. Lett.* **31**, 341–344.

Bischoff A. and Keil K. (1984) Al-rich objects in ordinary chondrites: Related origin of carbonaceous and ordinary chondrites and their consituents. *Geochim. Cosmochim. Acta* **48**, 693–709.

Bollard J., Connelly J.N., and Bizzarro M. (2015) Pb-Pb dating of individual chondrules from the CB_a chondrite Gujba: Assessment of the impact plume formation model. *Meteorit. Planet. Sci.* **50**, 1197–1216.

Brearley A.J. (2006) The action of water. In: Lauretta, D.S., McSween, H.Y.Jr., (Eds.), Meteorites and the Early Solar System II, Univ. of Arizona Press, Tucson, pp. 587-624.

Brigham C.A., Yabuki H., Ouyang Z., Murrell M.T., El Goresy A., and Burnett D.S. (1986) Silica-bearing chondrules and clasts in ordinary chondrites. *Geochim. Cosmochim. Acta* 50, 1655-1666.

Chaumard N., Defouilloy C., and Kita N.T. (2018) Oxygen isotope systematics of chondrules in the Murchison CM2 chondrite and implications for the CO–CM relationship. *Geochim. Cosmochim. Acta* **228**, 220–242.

Ciesla F.J. (2005) Chondrule-forming processes – an overview. In Chondrites and the Protoplanetary Disk (eds. A.N. Krot, E.R.D. Scott and B. Reipurth). Astronomical Society of the Pacific, San Francisco, CA, pp. 811–820.

Clayton R.N. and Mayeda T.K. (1999) Oxygen isotope studies of carbonaceous chondrites. *Geochim. Cosmochim. Acta* **63**, 2089–2104.

Clayton R.N., Onuma N., Grossman L., and Mayeda T.K. (1977) Distribution of the pre-solar component in Allende and other carbonaceous chondrites. *Earth Planet. Sci. Lett.* **34**, 209–224.

Connolly H.C.Jr. and Huss G.R. (2010) Compositional evolution of the protoplanetary disk: Oxygen isotopes of type-II chondrules from CR2 chondrites. *Geochim. Cosmochim. Acta* **74**, 2473–2483.

Davidson J., Krot A.N., Nagashima K., Hellebrand E., and Lauretta D.S. (2014) Oxygen isotope and chemical compositions of magnetite and olivine in the anomalous CK3 Watson 002 and ungrouped Asuka-881595 carbonaceous chondrites: Effects of parent body metamorphism. *Meteorit. Planet. Sci.* **49**, 1456–1474.

Doyle P.M., Jogo K., Nagashima K., Krot A.N., Wakita S., Ciesla F.J., and Hutcheon I.D. (2015) Early aqueous activity on the ordinary and carbonaceous chondrite parent bodies recorded by

fayalite *Nat. Commun.* **6**, 7444.
Farver J.R. (2010) Oxygen and hydrogen diffusion in minerals. In *Diffusion in Minerals and Melts*, vol. 72 (eds. Y. Zhang and D.J. Cherniak), Rev. Mineral. Geochem., pp. 447–507.
Fedkin A.V., Grossman L., Humayun M., Simon S.B., and Campbell A.J. (2015) Condensates from vapor made by impacts between metal-, silicate-rich bodies: Comparison with metal and chondrules in CB chondrites. *Geochim. Cosmochim. Acta* **164**, 236–261.
Friedrich J.M., Weisberg M.K., Ebel D.S., Biltz A.E.., Corbett B.M., Iotzov I.V., Khan W.S., and Wolman M.D. (2014) Chondrule size and related physical properties: A compilation and evaluation of current data across all meteorite groups. *Chem. Erde* **75**, 419–443.
Fujiya W., Sugiura N., Hotta H., Ichimura K., and Sano Y. (2012) Evidence for the late formation of hydrous asteroids from young meteoritic carbonates. *Nat. Commun.* **3**, 627.
Gounelle M., Young E.D., Shahar A., Tonui E., and Kearsley A. (2007) Magnesium isotopic constraints on the origin of CB_b chondrites. *Earth Planet. Sci. Lett.* **256**, 521–533.
Greshake A., Krot A.N., Meibom A., Weisberg M.K., and Keil K. (2002) Heavily-hydrated matrix lumps in the CH and metal-rich chondrites QUE 94411 and Hammadah al Hamra 237. *Meteorit. Planet. Sci.* **37**, 281–293.
Grossman J.N., Rubin A.E., and MacPherson G.J. (1988) ALH85085: a unique volatile-poor carbonaceous chondrite with possible implications for nebular fractionation processes. *Earth Planet. Sci. Lett.* **91**, 33–54.
Hartmann L. (2005) Astrophysical observations of disk evolution around solar mass stars. In Chondrites and the Protoplanetary Disk (eds Krot, A. N., Scott, E. R. D. & Reipurth, B.) pp. 131–144. (Astrophysical Society of the Pacific, in the press).
Heck P.R., Ushikubo T., Schmitz B., Kita N.T., Spicuzza M.J., and Valley J.W. (2010) A single asteroidal source for extraterrestrial Ordovician chromite grains from Sweden and China: High-precision oxygen three-isotope SIMS analysis. *Geochim. Cosmochim. Acta* **74**, 497–509.
Hernández J., Hartmann L., Megeath T., Gutermuth R., Muzerolle J., Calvet N., Vivas A.K., Briceño C., Allen L., Stauffer J., Young E., and Fazio G. (2007) A Spitzer Space Telescope study of disks in the young s Orionis cluster. *Astrophys. J.* **662**, 1067–1081.
Hertwig A.T., Defouilloy C., and Kita N.T. (2018) Formation of chondrules in a moderately high dust enriched disk: Evidence from oxygen isotopes of chondrules from the Kaba CV3 chondrite. *Geochim. Cosmochim. Acta* **224**, 116–131.
Hertwig A.T., Kimura M., Ushikubo T., Defouilloy C., and Kita N.T. (2019a) The ^{26}Al-^{26}Mg systematics of FeO-rich chondrules from Acfer 094: Two chondrule generations distinct in age and oxygen isotope ratios. *Geochim. Cosmochim. Acta* **253**, 111–126.
Hertwig A. T., Kimura M., Defouilloy C., and Kita N. T. (2019b) Oxygen isotope systematics of chondrule olivine, pyroxene, and plagioclase in one of the most pristine CV3Red chondrites Northwest Africa 8613. *Meteorit. Planet. Sci.* **54**, 2666–2685.
Hezel D.C., Palme H., Brenker F.E., and Nasdala L. (2003) Evidence for fractional condensation and reprocessing at high temperatures in CH chondrites. *Meteorit. Planet. Sci.* **38**, 1199–1215.
Hezel D.C., Palme H., Nasdala L., and Brenker F.E. (2006) Origin of SiO_2-rich components in ordinary chondrites. *Geochim. Cosmochim. Acta* **70**, 1548–1564.
Hezel D.C. and Parteli E. (2018) The spatial origin of chondrules in individual chondrites: constraints from modelling chondrule mixing. *Astrophys. J.* **863**, 54 (17pp).
Hezel D.C., Bland P.A., Palme H., Jacquet E., and Bigolski J. (2018) Composition of chondrules and matrix and their complementary relationship in chondrites. In: Chondrules: Records of Protoplanetary Disk Processes (Cambridge Planetary Science). Eds: S.S. Russell, H.C.

Connolly Jr. and A.N. Krot. Cambridge University Press, Cambridge UK, pp. 457.
Ikeda Y. (1980) Petrology of Allan Hills-764 chondrite (LL3). *Mem. Natl. Inst. Polar Res. Spec.* **17**, 50-82.
Ivanova M.A. and Petaev M.I. (2015) Characteristics and origin of the components of the carbonaceous chondrite NWA 470. *Petrology* **23**, 150–167.
Ivanova M.A., Kononkova N.N., Krot A.N., Greenwood R.C., Franchi I.A., Verchovsky A.B., Trieloff M., Korochantseva E.V., and Brandstätter F. (2008) The Isheyevo meteorite: Mineralogy, petrology, bulk chemistry, oxygen, nitrogen, carbon isotopic compositions, and ^{40}Ar-^{39}Ar ages. *Meteorit. Planet. Sci.* **43**, 915–940.
Jilly-Rehak C.E., Huss G.R., Nagashima K., and Schrader D.L. (2018) Low-temperature aqueous alteration on the CR chondrite parent body: Implications from in situ oxygen-isotope analyses. *Geochim. Cosmochim. Acta* **222**, 230–252.
Jones R.H. (2012) Petrographic constraints on the diversity of chondrule reservoirs in the protoplanetary disk. *Meteoriti. Planet. Sci.* **47**, 1176–1190.
Kita N.T., Ushikubo T., Fu B., and Valley J.W. (2009) High precision SIMS oxygen isotope analysis and the effect of sample topography. *Chem. Geol.* **264**, 43–57.
Kita N.T., Nagahara H., Tachibana S., Tomomura S., Spicuzza M.J., Fournelle J.H., and Valley J.W. (2010) High precision SIMS oxygen three isotope study of chondrules in LL3 chondrites: Role of ambient gas during chondrule formation. *Geochim. Cosmochim. Acta* **74**, 6610–6635.
Kobayashi S., Imai H., and Yurimoto H. (2003) New extreme 16O-rich reservoir in the early solar system. *Geochem. J.* **37**, 663–669.
Krot A.N., Meibom A., Petaev M.I., Keil K., Zolensky M.E., Saito A., Mukai M., and Ohsumi K. (2000) Ferrous silicate spherules with euhedral iron-nickel metal grains from CH carbonaceous chondrites: Evidence for supercooling and condensation under oxidizing conditions. *Meteorit. Planet. Sci.* **35**, 1249–1258.
Krot A.N., Meibom A., Russell S.S., Alexander C.M.O'D., Jeffries T.E., and Keil K. (2001a) A new astrophysical setting for chondrule formation. *Science* **291**, 1776–1779.
Krot A.N., McKeegan K.D., Russell S.S., Meibom A., Weisberg M.K., Zipfel J., Krot T.V., Fagan T. J., and Keil K. (2001b) Refractory Ca, Al-rich inclusions and Al-diopside-rich chondrules in the metal-rich chondrites Hammadah al Hamra 237 and QUE 94411. *Meteorit. Planet. Sci.* **36**, 1189–1217.
Krot A.N., Meibom A., Weisberg M.K., and Keil K. (2002) The CR chondrite clan: Implications for early solar system processes. *Meteorit. Planet. Sci.* **37**, 1451–1490.
Krot A.N., Libourel G., Goodrich C.A., and Petaev M.I. (2004) Silica-rich igneous rims around magnesian chondrules in CR carbonaceous chondrites: Evidence for condensation origin from fractionated nebular gas. *Meteorit. Planet. Sci.* **39**, 1931–1955.
Krot A.N., Amelin Y., Cassen P., and Meibom A. (2005) Young chondrules in CB chondrites from a giant impact in the early Solar System. *Nature* **436**, 989–992.
Krot A.N., Ivanova M.A., and Ulyanov A.A. (2007) Chondrules in the CB/CH-like carbonaceous chondrite Isheyevo: Evidence for various chondrule-forming mechanisms and multiple chondrule generations. *Chem. Erde* **67**, 283–300.
Krot A.N., Amelin Y., Bland P., Ciesla F.J., Connelly J., Davis A.M., Huss G.R., Hutcheon I.D., Makide K., Nagashima K., Nyquist L.E., Russell S.S., Scott E.R.D., Thrane K., Yurimoto H., and Yin Q.-Z. (2009) Origin and chronology of chondritic components: A review. *Geochim. Cosmochim. Acta* **73**, 4963–4997.

Krot A.N., Nagashima K., Yoshitake M., and Yurimoto H. (2010) Oxygen isotopic compositions of chondrules from the metal-rich chondrites Isheyevo (CH/CB_b), MAC 02675 (CB_b) and QUE 94627 (CB_b). *Geochim. Cosmochim. Acta* **74**, 2190–2211.

Krot A.N., Nagashima K., and Petaev M.I. (2012) Isotopically uniform, ^{16}O-depleted calcium, aluminum-rich inclusions in CH and CB carbonaceous chondrites. *Geochim. Cosmochim. Acta* **83**, 159–178.

Krot A.N., Dobrica E., Petaev M., Nagashima K., and Brearley A. (2014) Impact plume origin of ferroan chondrules in CH carbonaceous chondrites. *Meteorit. Planet. Sci.* **49**, A5195 (abstr.).

Krot A.N. and Nagashima K. (2017) Constraints on mechanisms of chondrule formation from chondrule precursors and chronology of transient heating events in the protoplanetary disk. *Geochem. J.* **51**, 45–68.

Krot A.N., Nagashima K., van Kooten E.M.M., and Bizzarro M. (2017a) High-temperature rims around calcium-aluminum-rich inclusions from the CR, CB and CH carbonaceous chondrites. *Geochim. Cosmochim. Acta*, **201**, 155–184.

Krot A.N., Nagashima K., van Kooten E. M. M., and Bizzarro M. (2017b) Calcium-aluminum-rich inclusions recycled during formation of porphyritic chondrules from CH carbonaceous chondrites. *Geochim. Cosmochim. Acta*, **201**, 185–223.

Marrocchi Y. and Chaussidon M. (2015) A systematic for oxygen isotopic variation in meteoritic chondurles. *Earth Planet. Sci. Lett.* **430**, 308–315.

Marrocchi Y., Villeneuve J., Batanova V., Piani L., and Jacquet E. (2018) Oxygen isotopic diversity of chondrule precursors and the nebular origin of chondrules. *Earth Planet. Sci. Lett.* **496**, 132–141.

Marrocchi Y., Euverte R., Villeneuve J., Batanova V., Welsch B., Ferrière L., and Jacquet E. (2019) Formation of CV chondrules by recycling of amoeboid olivine aggregate-like precursors. *Geochim. Cosmochim. Acta* **247**, 121–141.

Nakamura T., Noguchi T., and Akaki T. (2006) Mineralogy and oxygen isotope signatures of the Asuka 881020 CH chondrite. *Meteorit. Planet. Sci.* **41**(Suppl.), A128 (abstr.).

Nakashima D., Ushikubo T., Rudraswami N.G., Kita N.T., Valley J.W., and Nagao K. (2011) Ion microprobe analyses of oxygen three-isotope ratios of chondrules from the Sayh al Uhaymir 290 CH chondrite using a multiple-hole disk. *Meteorit. Planet. Sci.* **46**, 857–874.

Noguchi T., Imae N., and Kimura M. (2004) Petrology and mineralogy of Asuka 881020: A preliminary report of the first CH chondrite found among the Japanese Antarctic meteorite collection. In *Proc. NIPR Symp. Antarct. Meteorites*, **28**, 62–63 (abstr.).

Noguchi T., Nakamura T., Kimura M., Bischoff A., Osawa T., and Imae N. (2005) Mineralogy of heavily hydrated clasts in Asuka 881020, Acfer 182, and NWA 470 CH chondrites. In *Proc. NIPR Symp. Antarct. Meteorites*, **29**, 55–56 (abstr.).

Oulton J., Humayun M., Fedkin A., and Grossman L. (2016) Chemical evidence for differentiation, evaporation and recondensation from silicate clasts in Gujba. *Geochim. Cosmochim. Acta* **177**, 254–274.

Petaev M.I. and Wood J.A. (1998) The condensation with partial isolation (CWPI) model of condensation in the solar nebula. *Meteorit. Planet. Sci.* **33**, 1123–1137.

Petaev M.I., Meibom A., Krot A.N., Wood J.A., and Keil K. (2001) The condensation origin of zoned grains in QUE 94411: implications for the formation of the Bencubbin-like chondrites. *Meteorit. Planet. Sci.* **36**, 93–107.

Rudraswami N.G., Ushikubo T., Nakashima D., and Kita N.T. (2011) Oxygen isotope systematics of chondrules in Allende CV3 chondrite: High precision ion microprobe studies.

Geochim. Cosmochim. Acta **75**, 7596–7611.
Russell S.D.J., Longstaffe F.J., King P.L., and Larson T.E. (2010) The oxygen-isotope composition of chondrules and isolated forsterite and olivine grains from the Tagish Lake carbonaceous chondrite. *Geochim. Cosmochim. Acta* **74**, 2428–2499.
Sanders I.S. and Scott E.R.D. (2018) Making chondrule by splashing molten planetesimals: The dirty impact plume model. In *Chondrules: Records of Protoplanetary Disk Processes,* edited by S. S. Russell, H. C. Connolly Jr., and A. N. Krot, pp. 361 – 374. Cambridge Planetary Science, edited by F. Bagenal, D. Jewitt, C. Murray, J. Bell, R. Lorenz, F. Nimmo, S. Russell. Cambridge University Press.
Schrader D.L., Connolly H.C.Jr., Lauretta D.S., Nagashima K., Huss G.R., Davidson J., and Domanik K.J. (2013) The formation and alteration of the Renazzo-like carbonaceous chondrites II: linking O-isotope composition and oxidation state of chondrule olivine. *Geochim. Cosmochim. Acta* **101**, 302–327.
Schrader D.L., Nagashima K., Krot A.N., Ogliore R.C., and Hellebrand E. (2014) Variations in the O-isotope compositions of gas during the formation of chondrules from the CR chondrites. *Geochim. Cosmochim. Acta* **132**, 50–74.
Schrader D.L., Nagashima K., Krot A.N., Ogliore R.C., Yin Q.-Z., Amelin Y.A., Stirling C.H., and Kaltenbach A. (2017) Distribution of ^{26}Al in the CR chondrite chondrule-forming region of the protoplanetary disk. *Geochim. Cosmochim. Acta* **201**, 275–302.
Scott E.R.D. (1988) A new kind of primitive chondrite, Allan Hills 85085. *Earth Planet. Sci. Lett.* **91**, 1–18.
Scott E.R.D. and Krot A.N. (2003) Chondrites and their components. In *Meteorites, Comets, and Planets,* vol. 1, edited by A. M. Davis, pp. 143-200. Treatise on Geochemistry, edited by H. D. Holland and K. K. Turekian. Elsevier B. V., Amsterdam.
Scott E.R.D. and Krot A.N. (2005) Chondritic meteorites and the high-temperature nebular origins of their components. In A.N. Krot, E.R.D. Scott, and B. Reipurth (Eds.), Chondrites and the Protoplanetary Disk, 15–53. ASP Conf. Ser. 341. San Francisco, CA: Astronomical Society of the Pacific.
Tenner T.J., Ushikubo T., Kurahashi E., Nagahara H., and Kita N.T. (2013) Oxygen isotope systematics of chondrule phenocrysts from the CO3.0 chondrite Yamato 81020: evidence for two distinct oxygen isotope reservoirs. *Geochim. Cosmochim. Acta* **102**, 226–245.
Tenner T.J., Nakashima D., Ushikubo T., Kita N.T., and Weisberg M.K. (2015) Oxygen isotope ratios of FeO-poor chondrules in CR3 chondrites: Influence of dust enrichment and H_2O during chondrule formation. *Geochim. Cosmochim. Acta* **148**, 228–250.
Tenner T.J., Kimura M., and Kita N.T. (2017) Oxygen isotope characteristics of chondrules from the Yamato-82094 ungrouped carbonaceous chondrite: Further evidence for common O-isotope environments sampled among carbonaceous chondrites. *Meteorit. Planet. Sci.* **52**, 268–294.
Tenner T.J., Ushikubo T., Nakashima D., Schrader D.L., Weisberg M.K., Kimura M., and Kita N.T. (2018) Oxygen isotope characteristics of chondrules from recent studies by secondary ion mass spectrometry. In *Chondrules: Records of Protoplanetary Disk Processes,* edited by S. S. Russell, H. C. Connolly Jr., and A. N. Krot, pp. 196 – 246. Cambridge Planetary Science, edited by F. Bagenal, D. Jewitt, C. Murray, J. Bell, R. Lorenz, F. Nimmo, S. Russell. Cambridge University Press.
Ushikubo T., Kimura M., Kita N.T., and Valley J.W. (2012) Primordial oxygen isotope reservoirs of the solar nebula recorded in chondrules in Acfer 094 carbonaceous chondrite. *Geochim.*

Cosmochim. Acta **90**, 242–264.
Valley J.W. and Kita N.T. (2009) In situ Oxygen Isotope Geochemistry by Ion Microprobe. Mineralogical Association of Canada Short Course vol. **41**, 19–63.
Weisberg M.K. and Kimura M. (2010) Petrology and Raman spectroscopy of high pressure phases in the Gujba CB chondrite and the shock history of the CB parent body. *Meteorit. Planet. Sci.* **45**, 873–884.
Weisberg M.K., Prinz M., and Nehru C.E. (1988) Petrology of ALH 85085: a chondrite with unique characteristics. *Earth Planet. Sci. Lett.* **91**, 19–32.
Weisberg M.K., Prinz M., Clayton R.N., Mayeda T.K., Grady M.M., and Pillinger C.T. (1995) The CR chondrite clan. *Proc. NIPR Symp. Antarct. Meteorites* **8**, 11–32.
Weisberg M.K., Prinz M., Clayton R.N., Mayeda T.K., Sugiura N., Zashu S., and Ebihara M. (2001) A new metal-rich chondrite grouplet. *Meteorit. Planet. Sci.* **36**, 401–418.
Yamanobe M., Nakamura T., and Nakashima D. (2018) Oxygen isotope reservoirs in the outer asteroid belt inferred from oxygen isotope systematics of chondrule olivines and isolated forsterite and olivine grains in Tagish Lake-type carbonaceous chondrites, WIS 91600 and MET 00432. *Polar Sci.* **15**, 29–38.
Young E.D. and Russell S.S. (1998) Oxygen reservoirs in the early solar nebula inferred from an Allende CAI. *Science* **282**, 452–455.

Table 1. Oxygen isotope ratios of non-porphyritic chondrules in Asuka-881020[a].

Chondrule type	Name	Spot #	$\delta^{18}O$ ± 2SD (‰)		$\delta^{17}O$ ± 2SD (‰)		$\Delta^{17}O$ ± 2SD (‰)		Mg#	Target	Al/Si/CI[c]	Ca/Si/CI[c]
MgCC	C1	1	0.35	0.30	-2.29	0.52	-2.47	0.42	98.1	$En_{94.9}Wo_{3.3}$	0.462	0.647
	C2	1	0.87	0.30	-1.86	0.34	-2.31	0.38	99.4	$En_{99.0}Wo_{0.4}$	0.052	0.068
	C3	1	1.17	0.44	-1.87	0.37	-2.48	0.21	98.8	$En_{98.2}Wo_{0.6}$	0.114	0.115
	C4	1	0.32	0.30	-2.01	0.34	-2.18	0.38	95.3	$En_{94.1}Wo_{1.3}$	0.216	0.287
	C5	1	-5.63	0.19	-8.99	0.38	-6.06	0.34	98.9	$En_{95.1}Wo_{3.9}$	0.141	0.699
	C6	1	0.95	0.30	-1.84	0.52	-2.33	0.42	96.1	$En_{93.5}Wo_{2.7}$	0.474	0.522
	C7	1	0.73	0.30	-1.63	0.52	-2.01	0.42	95.5	$En_{94.0}Wo_{1.6}$	0.270	0.304
	C8	1	0.02	0.82	-2.33	1.49	-2.34	1.51	93.9	$En_{90.7}Wo_{3.4}$	0.521	0.678
	C9	1	-7.14	0.30	-9.79	0.34	-6.07	0.38	97.5	$En_{96.5}Wo_{0.9}$	0.084	0.178
	C10	1	2.96	0.44	0.41	0.37	-1.13	0.21	97.1	$En_{94.7}Wo_{2.4}$	0.472	0.472
FeCC	C11	1	7.49	0.30	5.63	0.34	1.74	0.38	83.4	$En_{83.2}Wo_{0.2}$	0.041	0.048
	C12	1	7.73	0.44	5.42	0.37	1.40	0.21	78.3	$En_{75.6}Wo_{3.5}$	0.899	0.718
	C13	1	7.77	0.37	5.42	0.36	1.38	0.41	72.3	$En_{70.8}Wo_{2.0}$	0.485	0.396
	C14	1	8.01	0.37	5.29	0.36	1.13	0.41	64.2	$En_{64.0}Wo_{0.3}$	0.051	0.073
	C15	1	7.85	0.30	5.31	0.34	1.22	0.38	73.3	$En_{73.1}Wo_{0.2}$	< 0.023	0.047
	C16	1	7.22	0.30	5.54	0.52	1.78	0.42	67.0	$En_{67.0}Wo_{0.0}$	< 0.014	< 0.014
	C17	1	9.17	0.44	6.27	0.37	1.50	0.21	65.1	$En_{62.7}Wo_{3.6}$	0.587	0.671
SB-I	C18	1	6.27	1.03	4.19	1.73	0.93	1.98		$En_{84.1}Wo_{0.0}$		
		2	7.81	1.03	5.59	1.73	1.52	1.98		silica		
		Average	7.04	0.77	4.89	1.22	1.23	1.40	80.1		< 0.017	< 0.021
	C19	1	6.67	1.18	3.63	1.82	0.16	1.97		$En_{95.6}Wo_{0.1}$		
		2	11.51	1.18	6.82	1.82	0.84	1.97		silica		
		Average	Not calculated						92.3		< 0.018	< 0.023
	C20	1	6.72	1.18	4.72	1.82	1.23	1.97		$En_{91.4}Wo_{0.1}$		
		2	6.83	1.18	5.19	1.82	1.64	1.97		silica		
		Average	6.77	0.83	4.95	1.29	1.43	1.39	89.6		< 0.019	< 0.024
	C21	1	8.11	1.18	4.07	1.82	-0.15	1.97		$En_{78.1}Wo_{0.1}$		
		2	8.18	1.18	6.14	1.82	1.89	1.97		silica		
		Average	8.14	0.83	5.10	1.29	0.87	1.39	77.5		< 0.018	< 0.023
	C22	1	5.91	1.18	3.75	1.82	0.68	1.97		$En_{84.5}Wo_{0.1}$		
		2	10.94	1.18	5.53	1.82	-0.16	1.97		Cristobalite		
		Average	Not calculated						78.6		< 0.018	< 0.023
	C23	1	7.07	1.03	4.68	1.73	1.01	1.98		$En_{82.1}Wo_{0.5}$		
		2	8.31	1.03	4.92	1.73	0.60	1.98		silica		
		Average	7.69	0.73	4.80	1.22	0.80	1.40	75.7		0.034	0.033
	C24	1	5.79	1.03	5.22	1.73	2.22	1.98	82.8	$En_{82.7}Wo_{0.1}$	< 0.020	< 0.025
	C25	1	8.98	0.81	6.51	1.70	1.85	1.74		silica		
		2	6.55	0.81	5.88	1.70	2.47	1.74		$En_{59.1}Wo_{0.4}$		
		Average	7.77	1.21	6.19	1.21	2.16	1.23	58.5		0.010	0.015
	C26	1	8.34	1.03	6.76	1.73	2.42	1.98		$En_{66.2}Wo_{0.5}$		
		2	8.14	1.03	4.84	1.73	0.61	1.98		silica		
		Average	8.24	0.73	5.80	1.22	1.52	1.40	66.3		0.010	0.036
MB	C27	1	8.03	1.03	4.36	1.73	0.18	1.98	69.3	$En_{69.2}Wo_{0.1}$	< 0.022	< 0.027
	C28	1	9.07	1.03	6.37	1.73	1.65	1.98	66.2	$En_{66.1}Wo_{0.1}$	0.026	< 0.014
	C29	1	-34.10	0.81	-38.27	1.70	-20.54	1.74		$En_{91.6}Wo_{6.8}$		
		2	-34.74	0.81	-38.74	1.70	-20.68	1.74		$En_{91.6}Wo_{6.8}$		
		Average	-34.42	0.57	-38.51	1.21	-20.61	1.23	98.3		1.127	1.186
	C30	1	7.80	1.18	6.35	1.82	2.29	1.97	75.4	$En_{75.3}Wo_{0.1}$	0.039	0.019
SO	C31	1	0.42	0.37	-2.56	0.36	-2.78	0.41	93.2[b]	$Fo_{97.5}$	0.840	0.996
RP	C32	1	2.64	0.37	0.21	0.36	-1.16	0.41		$En_{80.3}Wo_{1.0}$		
		2	2.36	0.37	0.24	0.36	-0.98	0.41		$En_{73.9}Wo_{2.7}$		
		Average	2.50	0.26	0.23	0.26	-1.07	0.29	72.1[b]		0.572	0.977
SO	C33	1	0.64	0.44	-1.74	0.37	-2.07	0.21	96.3[b]	$En_{86.5}Wo_{10.2}$	1.994	1.954
Al-rich	C34	1	6.83	0.37	5.22	0.36	1.67	0.41	89.8[b]	$En_{69.0}Wo_{23.2}$	4.136	3.896
	C35	1	-5.98	0.82	-8.03	1.49	-4.92	1.51		Anorthite		
		2	-6.29	0.82	-9.73	1.49	-6.46	1.51		Anorthite		
		Average	-6.13	0.58	-8.88	1.06	-5.69	1.07	96.1[b]		4.586	6.502
	C36	1	-8.49	0.82	-10.37	1.49	-5.96	1.51		$En_{80.0}Wo_{19.5}$		
		2	-8.68	0.82	-10.76	1.49	-6.25	1.51		$Fo_{98.9}$		
		Average	-8.59	0.58	-10.57	1.06	-6.10	1.07	99.1[b]		2.950	4.888
	C37	1	-19.15	0.82	-22.17	1.49	-12.21	1.51		$En_{78.2}Wo_{19.8}$		
		2	-20.15	0.82	-22.18	1.49	-11.70	1.51		$En_{86.5}Wo_{13.8}$		
		3	-20.16	0.82	-22.38	1.49	-11.89	1.51		$En_{73.3}Wo_{26.2}$		
		Average	-19.82	0.47	-22.24	0.86	-11.94	0.87	99.3[b]		2.834	3.495

[a] The uncertainties associated with average values are twice the standard error of the mean (2SE).

[b] The Mg# are from defocused EPMA data.

[c] The refractory element abundances are from defocused EPMA data.

Table 2. Oxygen isotope ratios of lithic fragments in Asuka-881020[a].

Fragment type	Name	Spot #	$\delta^{18}O$ ± 2SD (‰)		$\delta^{17}O$ ± 2SD (‰)		$\Delta^{17}O$ ± 2SD (‰)		Mg#	Target	Al/Si/CI[c]	Ca/Si/CI[c]
MgCC-like	F1	1	0.01	0.30	-1.81	0.34	-1.82	0.38	96.9	$En_{91.8}Wo_{5.3}$	0.929	1.033
	F2	1	0.31	0.44	-2.18	0.37	-2.34	0.21	96.9	$En_{95.5}Wo_{1.4}$	0.209	0.274
	F3	1	0.41	0.37	-1.64	0.36	-1.85	0.41	96.5	$En_{90.5}Wo_{6.2}$	1.286	1.191
	F4	1	-0.06	0.30	-2.08	0.34	-2.05	0.38	98.2	$En_{95.6}Wo_{2.7}$	0.852	0.492
	F5	1	0.24	0.30	-2.63	0.52	-2.76	0.42	96.3	$En_{91.3}Wo_{5.1}$	0.926	1.001
	F6	1	1.50	0.30	-1.39	0.52	-2.17	0.42	92.6	$En_{89.6}Wo_{3.2}$	0.598	0.634
	F7	1	8.96	0.30	6.38	0.52	1.71	0.42	95.4	$En_{91.6}Wo_{3.9}$	0.707	0.648
	F8	1	0.71	0.44	-1.59	0.37	-1.96	0.21	91.7	$En_{87.4}Wo_{4.7}$	0.978	1.002
	F9	1	0.89	0.30	-1.96	0.34	-2.42	0.38	95.7	$En_{95.5}Wo_{0.2}$	< 0.021	0.043
	F10	1	0.67	0.44	-1.56	0.37	-1.91	0.21	96.3	$En_{95.7}Wo_{0.7}$	0.120	0.136
	F11	1	9.41	0.30	4.81	0.52	-0.08	0.42	96.1	$En_{94.8}Wo_{1.4}$	0.209	0.239
	F12	1	0.66	0.30	-2.14	0.34	-2.49	0.38	98.0	$En_{95.2}Wo_{2.9}$	0.455	0.544
	F13	1	0.72	0.37	-1.95	0.36	-2.33	0.41	98.9	$En_{96.7}Wo_{2.2}$	0.415	0.432
	F14	1	0.87	0.30	-2.09	0.34	-2.54	0.38	98.1	$En_{92.0}Wo_{6.2}$	1.248	1.202
	F15	1	-1.08	0.30	-2.53	0.34	-1.96	0.38	96.8	$En_{88.2}Wo_{8.9}$	0.881	1.047
	F16	1	0.07	0.37	-2.30	0.36	-2.34	0.41	94.4	$En_{93.3}Wo_{1.2}$	0.238	0.221
	F17	1	1.02	0.30	-1.63	0.34	-2.16	0.38	95.2	$En_{93.4}Wo_{1.8}$	0.345	0.377
	F18	1	-0.04	0.44	-2.05	0.37	-2.03	0.21	93.3	$En_{89.9}Wo_{3.6}$	0.713	0.542
	F19	1	-0.05	0.29	-2.30	0.66	-2.28	0.68	98.9	$En_{97.1}Wo_{1.9}$	0.458	0.365
	F20	1	0.95	0.29	-1.89	0.66	-2.38	0.68	98.9	$En_{97.0}Wo_{1.9}$	0.346	0.370
	F21	1	-0.29	0.29	-2.63	0.66	-2.49	0.68	98.4	$En_{96.6}Wo_{1.9}$	0.581	0.377
	F22	1	0.80	0.29	-1.59	0.66	-2.01	0.68	99.2	$En_{97.8}Wo_{1.4}$	0.300	0.273
	F23	1	2.55	0.29	0.57	0.66	-0.76	0.68	97.1	$En_{95.0}Wo_{2.1}$	0.422	0.415
	F24	1	-15.52	0.29	-18.57	0.66	-10.50	0.68	99.4	$En_{98.6}Wo_{0.8}$	0.064	0.156
	F25	1	0.74	0.29	-2.03	0.66	-2.42	0.68	98.9	$En_{97.2}Wo_{1.7}$	0.267	0.329
	F26	1	0.90	0.17	-1.68	0.63	-2.15	0.65	98.7	$En_{94.9}Wo_{3.9}$	0.605	0.761
	F27	1	4.08	0.17	1.98	0.63	-0.14	0.65	96.2	$En_{94.0}Wo_{2.3}$	0.363	0.417
	F28	1	1.32	0.17	-1.11	0.63	-1.80	0.65	98.4	$En_{95.8}Wo_{2.6}$	0.439	0.523
	F29	1	-14.99	0.17	-17.52	0.63	-9.72	0.65	98.9	$En_{96.3}Wo_{2.6}$	0.525	0.500
	F30	1	0.93	0.17	-2.07	0.63	-2.55	0.65	99.4	$En_{97.3}Wo_{2.1}$	0.370	0.417
	F31	1	0.95	0.17	-1.87	0.63	-2.36	0.65	99.4	$En_{98.4}Wo_{1.0}$	0.174	0.199
	F32	1	0.78	0.17	-2.02	0.63	-2.42	0.65	99.6	$En_{99.5}Wo_{0.1}$	< 0.040	< 0.041
	F33	1	0.47	0.17	-2.54	0.63	-2.79	0.65	99.3	$En_{99.2}Wo_{0.1}$	< 0.040	< 0.041
FeCC-like	F34	1	6.61	0.44	5.27	0.37	1.84	0.21	86.3	$En_{86.3}Wo_{0.0}$	< 0.020	< 0.025
	F35	1	6.67	0.29	5.24	0.66	1.77	0.68	77.2	$En_{77.2}Wo_{0.0}$	< 0.042	< 0.043
SB	F36	1	-5.77	1.03	-8.14	1.73	-5.14	1.98	95.8	$En_{92.8}Wo_{3.0}$		
		2	-3.88	1.03	-8.81	1.73	-6.79	1.98	95.2	$En_{63.4}Wo_{33.4}$		
		3	-3.63	1.03	-8.55	1.73	-6.66	1.98		Cristobalite		
		Average	-4.42	0.68	-8.50	1.00	-6.20	1.14	91.1[b]		1.672	1.856
	F37	1	-2.14	0.44	-4.56	0.37	-3.44	0.21	95.1	$En_{90.6}Wo_{4.5}$	0.496	0.522
	F38	2[d]	-3.97	1.18	-5.93	1.82	-3.87	1.97	86.6[b]	$En_{84.7}Wo_{5.5}$	0.436	0.516
	F39	1	15.47	0.81	13.56	1.70	5.52	1.74		Pl + Px		
		2	15.88	0.81	12.90	1.70	4.64	1.74		Cristobalite		
		3	16.31	0.81	13.71	1.70	5.23	1.74		Pl + Px		
		Average	15.89	0.47	13.39	0.98	5.13	1.00	82.5[b]		1.317	1.228
SB-I	F40	1	14.79	1.03	9.73	1.73	2.04	1.98		$En_{61.7}Wo_{0.2}$		
		2	13.34	1.03	9.34	1.73	2.40	1.98		$En_{58.4}Wo_{0.2}$		
		3	15.07	1.03	11.43	1.73	3.60	1.98		Cristobalite		
		Average	14.40	0.60	10.17	1.00	2.68	1.14	55.3[b]		0.043	< 0.017

[a] The uncertainties associated with average values are twice the standard error of the mean (2SE).

[b] The Mg# are from defocused EPMA data.

[c] The refractory element abundances are from defocused EPMA data.

[d] The analysis of the spot #1 in F38 is rejected because it overlapped with a crack in F38.

Table 3. Numbers of individual non-porphyritic chondrule types classified into the three groups

	SO	RP	MgCC (incl. LF)	FeCC (incl. LF)	MB	SB (incl. LF)	Al-rich	Totals
–2.3‰ group	2[a]	-	89	-	-	-	-	91
+1.4‰ group	-	-	1	11	3 (FeO-rich)	10 (FeO-rich; immiscibility texture)	1 (FeO-rich)	26
–6.3‰ group	-	-	3	-	-	2	5	10
Others	-	1 (FeO-rich)	7	-	1	3 (FeO-rich & -poor)	1	13
Totals	2	1	100	11	4	15	7	140

[a] More SO chondrules that can be classified into the –2.3‰ group are reported in Krot and Nagashima (2017).

1

2

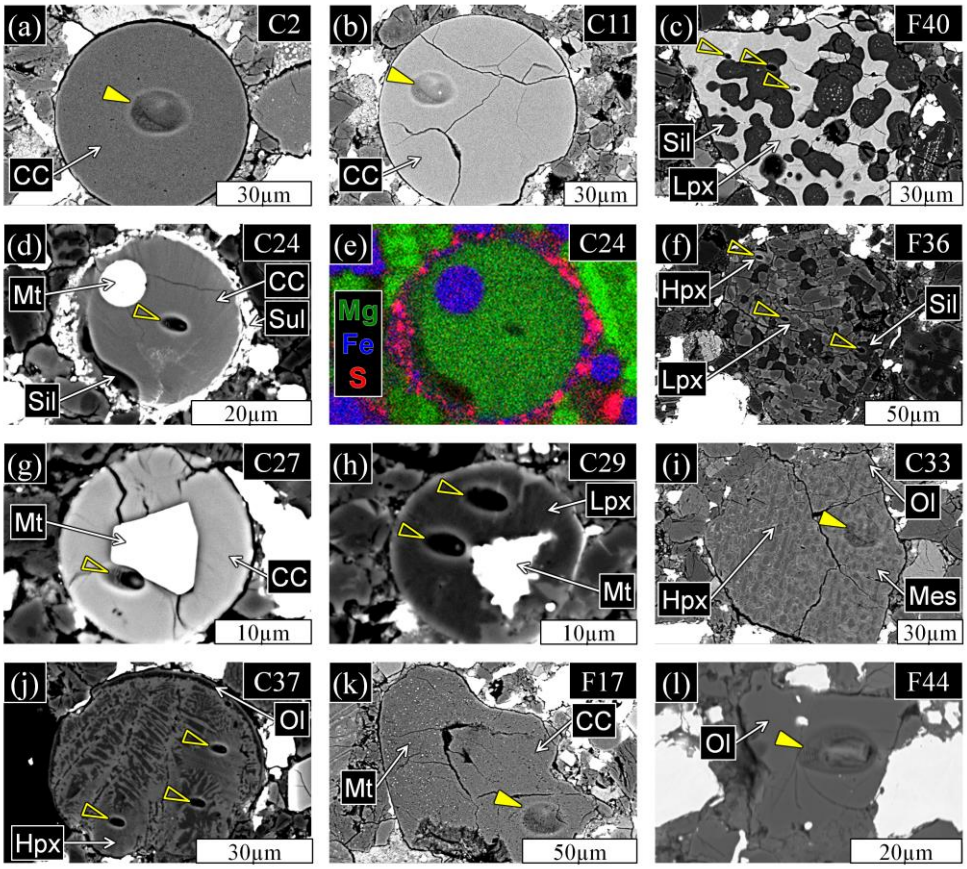

Fig. 1: BSE images and a combined elemental map of chondrules and isolated grains in Asuka-881020 after oxygen isotope analyses; (a) C2, a MgCC chondrule, (b) C11, a FeCC chondrule, (c) F40, a SB-I lithic fragment, (d) C24, a SB-I chondrule, (e) a combined elemental map in Mg (green), Fe (blue), and S (red) X-rays of C24, (f) F36, a SB lithic fragment, (g) C27, a FeO-rich MB chondrule, (h) C29 a FeO-poor MB chondrule, (i) C33, a SO chondrule, (j) C37, an Al-rich chondrule, (k) F17, a MgCC-like lithic fragment, and (l) F44, an olivine fragment. Analysis points are shown by the vertex of a filled triangle for 15 μm spot and that of an open triangle for 4 μm spot. Abbreviations: CC, cryptocrystalline olivine-pyroxene normative material; Sil, silica; Sul, Fe-sulfide; Mt, FeNi metal; Lpx, low-Ca pyroxene; Ol, olivine; Hpx, high-Ca pyroxene; Mes, mesostasis.

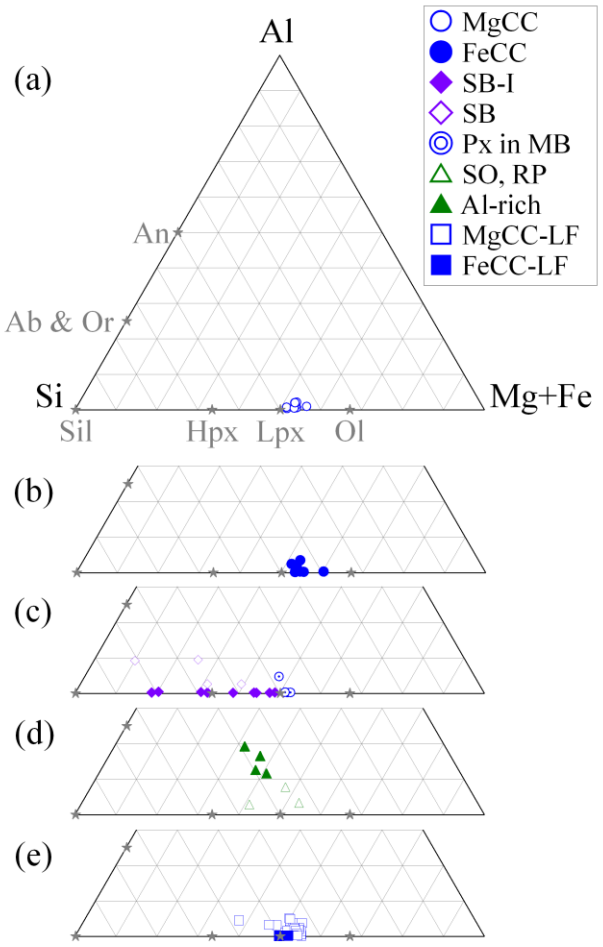

Fig. 2: Electron microprobe analyses of non-porphyritic chondrules and lithic fragments in Asuka-881020 in terms of atomic ratios of Si, Al, and (Mg+Fe). Also shown are stoichiometric olivine (Ol), low-Ca pyroxene (Lpx), high-Ca pyroxene (Hpx), feldspar [anorthite (An), albite (Al), and orthoclase (Or)], and silica (Sil).

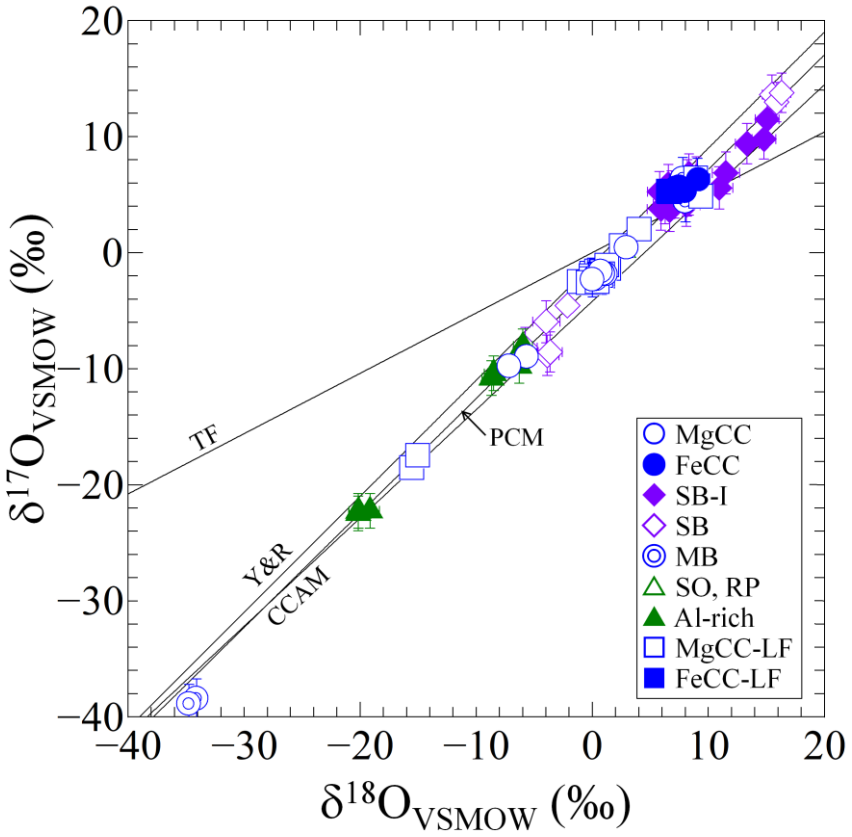

Fig. 3: Oxygen three-isotope ratios of the non-porphyritic chondrules and lithic fragments in Asuka-881020. TF, Y&R, PCM, and CCAM represent the terrestrial fractionation line, the Young and Russell line, the Primitive Chondrule Mineral line and the Carbonaceous Chondrite Anhydrous Mineral line.

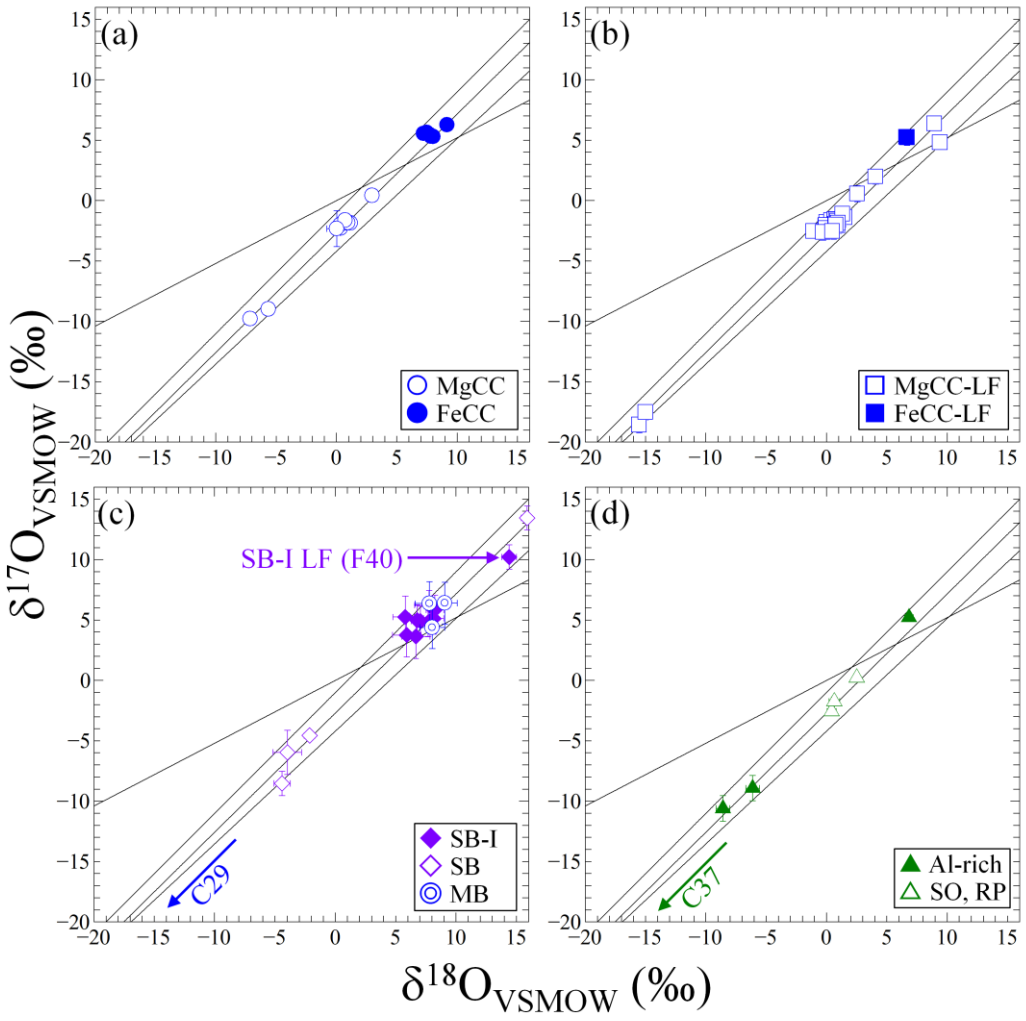

Fig. 4: Oxygen three-isotope ratios of CC chondrules (a), CC-like lithic fragments (b), SB-I chondrules, SB-I lithic fragment, SB lithic fragments, and MB chondrules (c), and Al-rich, SO, and RP chondrules (d). In panels c and d, average oxygen isotope ratios of individual chondrules are plotted.

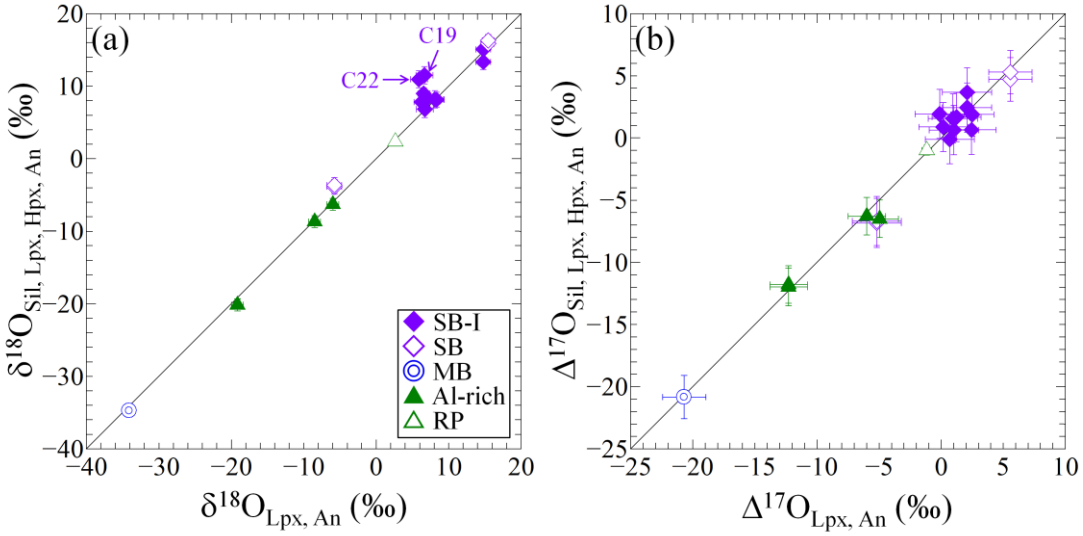

Fig. 5: Comparison between oxygen isotope ratios of low-Ca pyroxene (or anorthite) and other mineral phases in the same chondrules and lithic fragments: (a) $\delta^{18}O$ and (b) $\Delta^{17}O$. In panel a, most data plot on 1:1 line, though two data from the SB-I chondrules (C19 and C22) plot above the 1:1 line exceeding the uncertainty.

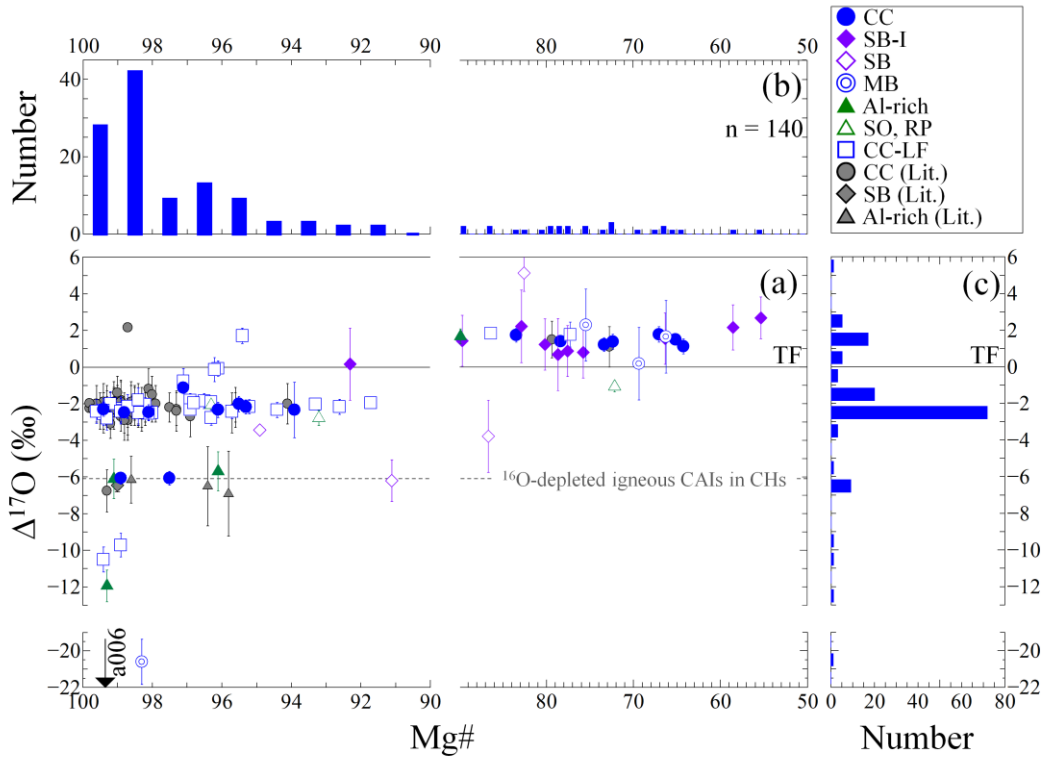

Fig. 6: (a) Comparison between $\Delta^{17}O$ values and Mg# of the non-porphyritic chondrules and lithic fragments, (b) Mg# histogram of the non-porphyritic chondrules and lithic fragments, and (c) $\Delta^{17}O$ histogram of the non-porphyritic chondrules and lithic fragments. Literature data of the non-porphyritic chondrules are from Krot et al. (2001b, 2010, 2012), Kobayashi et al. (2003), and Nakashima et al. (2011). In panel a, the dashed line at $\Delta^{17}O$ of ~ –6‰ is from the ^{16}O-depleted igneous CAIs in CH chondrites (Krot et al., 2012).

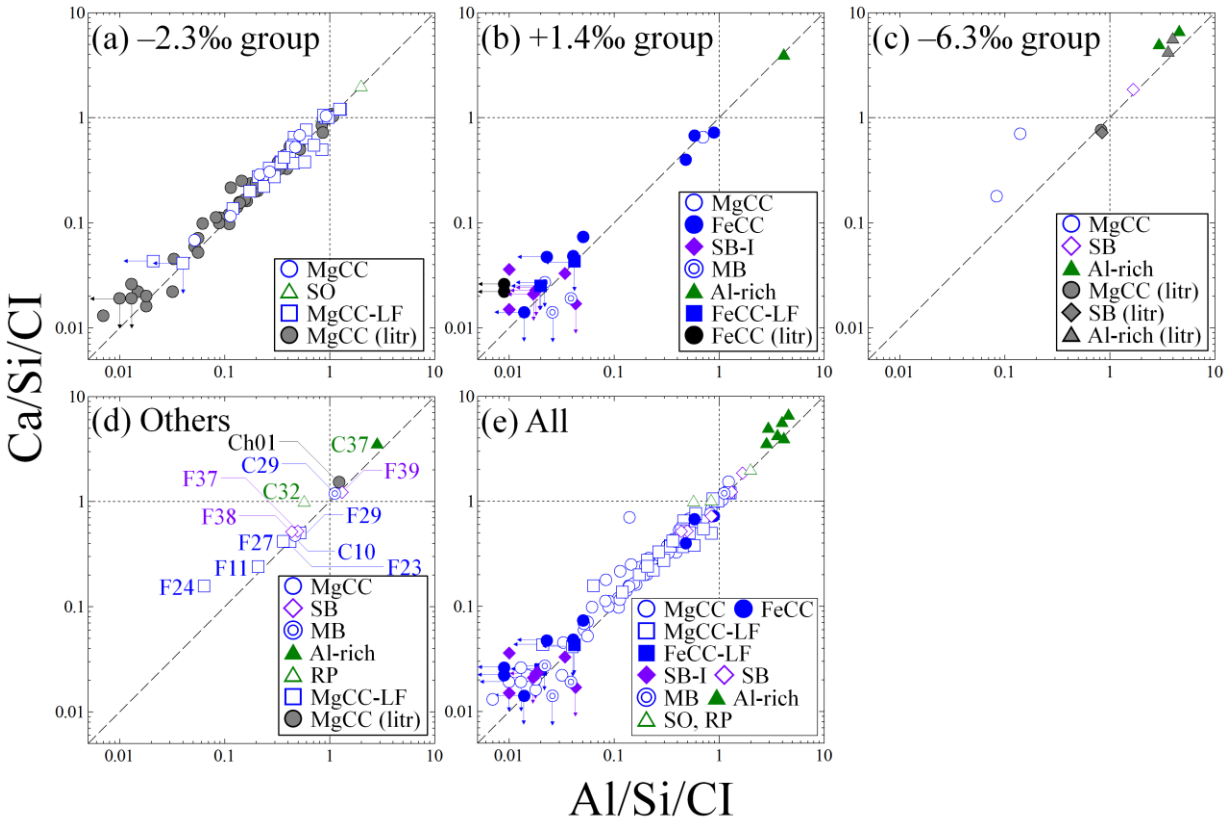

Fig. 7: Bulk refractory element compositions of the non-porphyritic chondrules and lithic fragments normalized by Si and elemental abundances of CI chondrites (Anders and Grevesse, 1989) in log scale; (a) the –2.3‰ group, (b) the +1.4‰ group, (c) the –6.3‰ group, (d) other objects that are not included in one of the three groups, and (e) all the non-porphyritic chondrules and fragments. Literature data of the non-porphyritic chondrules are from Krot et al. (2001b, 2010) and Nakashima et al. (2011). The dashed lines represent the 1:1 line. The dotted lines in a horizontal direction correspond to the CI's Ca/Si ratio, and those in a vertical direction correspond to the CI's Al/Si ratio. In panel e, chondrules having the same textural and chemical characteristics are expressed as the same legends, regardless of the present study or previous studies.

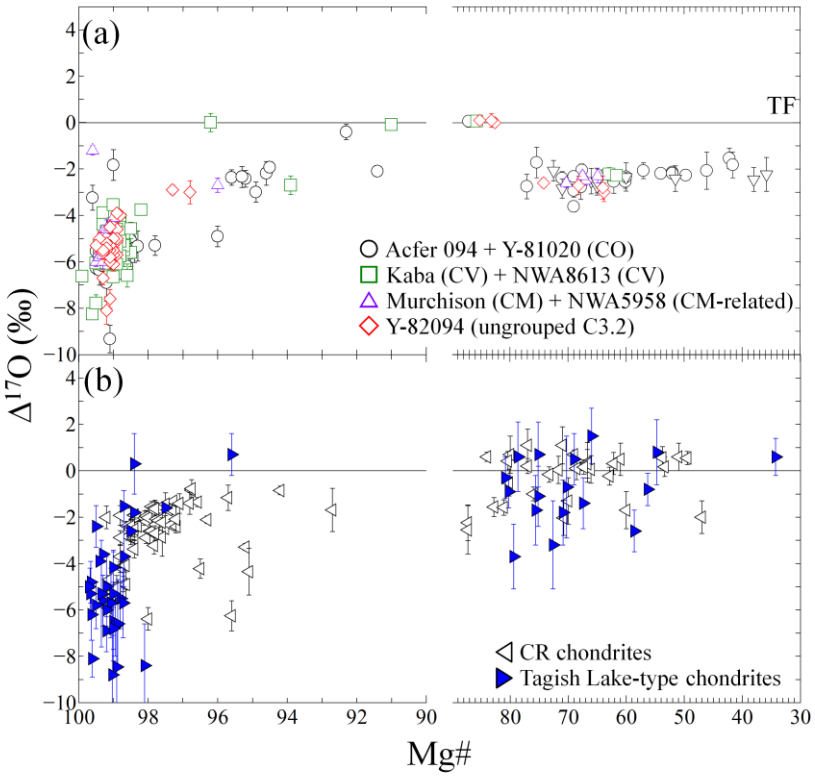

Fig. 8: Comparison between $\Delta^{17}O$ values and Mg# of chondrules from Acfer 094 (ungrouped C3.0), Yamato-81020 (CO3.0), Kaba (CV3), Northwest Africa (NWA) 8613 (CV3), Murchison (CM), NWA 5858 (CM-related), and Yamato-82094 (ungrouped C3.2) (a) and chondrules from CR chondrites and Tagish Lake-type chondrites (b). Literature data are from Connolly and Huss (2010), Russell et al. (2010), Ushikubo et al. (2012), Schrader et al. (2013, 2014, 2017), Tenner et al. (2013, 2015, 2018), Chaumard et al. (2018), Hertwig et al. (2018, 2019a, 2019b), Yamanobe et al. (2018), Marrocchi et al. (2018, 2019).

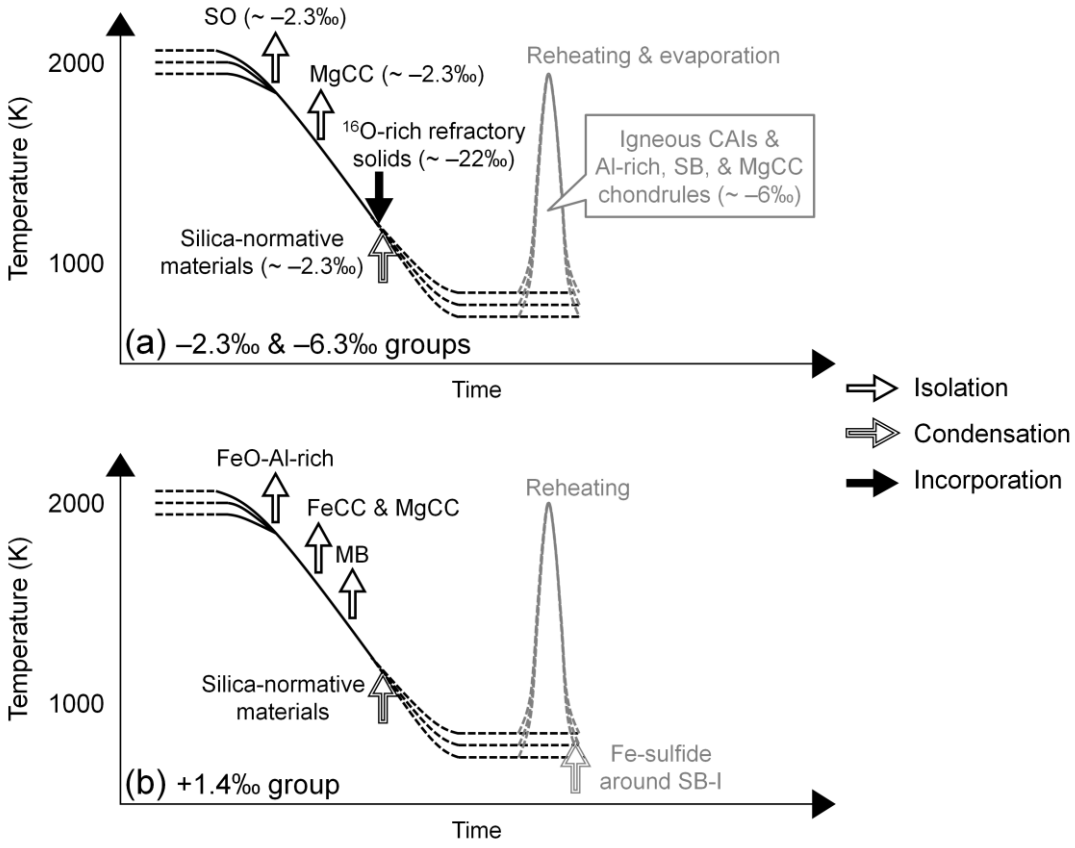

Fig. 9: Possible formation sequences for the non-porphyritic chondrules and lithic fragments in CH and CB chondrites; (a) the –2.3‰ group objects and –6.3‰ group objects and (b) the +1.4‰ group objects (after Fig. 11 in Hezel et al., 2003). Dashed lines represent temperatures that are uncertain. The reheating events and their products are drawn in gray to distinguish the preceding heating events and their products, as the reheating events were localized and did not affect all the chondrules and fragments.